[44] W. Zhou, J. Shao, Q. Jin, Q. Wei, J. Tang, J. Ji, Chem. Commun. 46 (2010) 1479–1481.
[45] J. Qiao, L. XiangSheng, X. JianPing, J. Jian, S. JiaCong, Sci. China Ser. B-Chem. 52 (2009) 64–68.
[46] Y.-C. Chung, I.-H. Chen, C.-J. Chen, Biomaterials 29 (2008) 1807–1816.
[47] R. Matsuno, K. Ishihara, Trans. Mater. Res. Soc. Jpn. 32 (2007) 555–558.
[48] J.J. Yuan, S.P. Armes, Y. Takabayashi, K. Prassides, C.A.P. Leite, F. Galembeck, A.L. Lewis, Langmuir 22 (2006) 10989–10993.
[49] B. Dubertret, P. Skourides, D.J. Norris, V. Noireaux, A.H. Brivanlou, A. Libchaber, Science 298 (2002) 1759–1762.
[50] R. Narain, A. Housni, L. Lane, J. Polym. Sci. Part A: Polym. Chem. 44 (2006) 6558–6568.
[51] A.B. Artyukhin, A. Shestakov, J. Harper, O. Bakajin, P. Stroeve, A. Noy, J. Am. Chem. Soc. 127 (2005) 7538–7542.
[52] A.-L. Troutier, L. Véron, T. Delair, C. Pichot, C. Ladavière, Langmuir 21 (2005) 9901–9910.
[53] A.-L. Troutier, T. Delair, C. Pichot, C. Ladavière, Langmuir 21 (2005) 1305–1313.
[54] I. De Miguel, L. Imbertie, V. Rieumajou, M. Major, R. Kravtzoff, D. Betbeder, Pharm. Res. 17 (2000) 817–824.
[55] D. Samanta, S. McRae, B. Cooper, Y. Hu, T. Emrick, J. Pratt, S.A. Charles, Biomacromolecules 9 (2008) 2891–2897.
[56] R. Kojima, M.C.Z. Kasuya, K. Ishihara, K. Hatanaka, Polym. J. 41 (2009) 1–4.
[57] K.L. Thompson, I. Bannister, S.P. Armes, A.L. Lewis, Langmuir 26 (2010) 4693–4702.
[58] Y. Iwasaki, K. Akiyoshi, Biomacromolecules 7 (2006) 1433–1439.
[59] J.P. Xu, J. Ji, W.D. Chen, J.C. Shen, J. Control. Release 107 (2005) 502.
[60] C. Allen, D. Maysinger, A. Eisenberg, Colloids Surf. B: Biointerfaces 16 (1999) 3–27.
[61] L. Yang, P. Alexandridis, Colloids Interface Sci. 5 (2000) 132–143.
[62] A. Rosler, G.W.M. Vandermeulen, H.A. Klok, Adv. Drug Deliv. Rev. 53 (2001) 95–108.
[63] A. Harada, K. Kataoka, Science 283 (1999) 65–67.
[64] T. Ueda, H. Oshida, K. Kurita, K. Ishihara, N. Nakabayashi, Polym. J. 24 (1992) 1259–1269.
[65] K. Ishihara, Y. Iwasaki, N. Nakabayashi, Polym. J. 31 (1999) 1231–1236.
[66] T. Goda, Y. Goto, K. Ishihara, Biomaterials 31 (2010) 2380–2387.
[67] T. Konno, J. Watanabe, K. Ishihara, J. Biomed. Mater. Res. A 65 (2003) 209–214.
[68] M. Wada, H. Jinno, M. Ueda, T. Ikeda, M. Kitajima, T. Konno, J. Watanabe, K. Ishihara, Anticancer Res. 27 (2007) 1431–1435.
[69] D. Soma, J. Kitayama, T. Konno, K. Ishihara, J. Yamada, T. Kamei, H. Ishigami, S. Kaisaki, H. Nagawa, Cancer Sci. 100 (2009) 1979–1985.
[70] V.J. Dzau, R.C. Braun-Dullaeus, D.G. Sedding, Nat. Med. 8 (2002) 1249–1256.
[71] G.M. Ferron, W.J. Jusko, Drug Metab. Dispos. 26 (1998) 83–84.
[72] H.I. Kim, M. Takai, T. Konno, R. Matsuno, K. Ishihara, Drug Deliv. 16 (2009) 183–188.
[73] K. Takei, T. Konno, J. Watanabe, K. Ishihara, Biomacromolecules 9 (2004) 858–862.
[74] R. Miyata, M. Ueda, H. Jinno, T. Konno, K. Ishihara, N. Ando, Y. Kitagawa, Int. J. Cancer 124 (2009) 2460–2467.
[75] T. Shimada, M. Ueda, H. Jinno, N. Chiba, M. Wada, J. Watanabe, K. Ishihara, Y. Kitagawa, Anticancer Res. 29 (2009) 1009–1014.
[76] N. Chiba, M. Ueda, T. Shimada, H. Jinno, J. Watanabe, K. Ishihara, M. Kitajima, Eur. Surg. Res. 39 (2007) 103–110.
[77] Y. Iwasaki, H. Maie, K. Akiyoshi, Biomacromolecules 8 (2007) 3162–3168.
[78] J.P. Salvage, S.F. Rose, G.J. Phillips, G.W. Hanlon, A.W. Lloyd, I.Y. Ma, S.P. Armes, N.C. Billingham, A.L. Lewis, J. Control. Release 104 (2005) 259–270.
[79] M. Licciarde, Y. Tang, N.C. Billingham, S.P. Armes, A.L. Lewis, Biomacromolecules 6 (2005) 1085–1096.
[80] M. Wu, W. Gunning, M. Ratman, Cancer Epidemiol. Biomarkers Prev. 8 (1999) 775–782.
[81] M. Licciarde, G. Giammona, J. Du, S.P. Armes, Y. Tang, A.L. Lewis, Polymer 47 (2006) 2946–2955.
[82] M. Licciarde, E.F. Craparo, G. Giammona, S.P. Armes, Y. Tang, A.L. Lewis, Macromol. Biosci. 8 (2008) 615–626.
[83] J.P. Xu, J. Ji, W.D. Chen, J.C. Shen, J. Control. Release 107 (2005) 502–512.
[84] J.P. Xu, J. Ji, W.D. Chen, J.C. Shen, Macromol. Biosci. 5 (2005) 164–171.
[85] N. Chiba, M. Ueda, T. Shimada, H. Jinno, J. Watanabe, K. Ishihara, M. Kitajima, Eur. Surg. Res. 39 (2007) 23–34.
[86] Y.T.A. Chim, J.K.W. Lam, Y. Ma, S.P. Armes, A.L. Lewis, C.J. Roberts, S. Stolnik, S.J.B. Tendler, M.C. Davies, Langmuir 21 (2005) 3591–3598.
[87] J.K.W. Lam, Y. Ma, S.P. Armes, A.L. Lewis, T. Baldwin, S. Stolnik, J. Control. Release 100 (2004) 293–312.
[88] X. Zhao, Z. Zhang, F. Pan, Y. Ma, S.P. Armes, A.L. Lewis, J.R. Lu, Surf. Interface Anal. 38 (2006) 548–551.
[89] J.K.W. Lam, S.P. Armes, A.L. Lewis, S. Stolnik, J. Drug Target. 17 (2009) 512–523.
[90] T. Kitagawa, R. Iwase, K. Ishihara, T. Yamaoka, A. Murakami, Chem. Lett. 34 (2005) 1478–1479.
[91] A.M. Funhoff, C.F. van Nostrum, G.A. Koning, N.M. Schuurmans-Nieuwenbroek, D.J.A. Crommelin, W.E. Hennink, Biomacromolecules 5 (2004) 32–39.
[92] K. Kogure, H. Akita, Y. Yamada, H. Harashima, Adv. Drug Deliv. Rev. 60 (2008) 559–571.
[93] K. Sasaki, K. Kogure, S. Chaki, Y. Nakamura, R. Moriguchi, H. Hamada, M. Ueno, S. Futaki, H. Harashima, Anal. Bioanal. Chem. 391 (2008) 2717–2727.
[94] M. Ukawa, H. Akita, T. Masuda, Y. Hayashi, T. Konno, K. Ishihara, H. Harashima, Biomaterials 31 (2010) 6355–6362.
[95] K. Nishizawa, T. Konno, M. Takai, K. Ishihara, Biomacromolecules 9 (2008) 403–407.
[96] K. Sakai-Kato, M. Kato, K. Ishihara, T. Toyo'oka, Lab Chip 4 (2004) 4–6.
[97] J. Park, S. Kurosawa, M. Takai, K. Ishihara, Colloids Surf. B: Biointerfaces 55 (2007) 164–172.
[98] Y. Goto, R. Matsuno, T. Konno, M. Takai, K. Ishihara, Biomacromolecules 9 (2008) 828–833.
[99] J. Watanabe, K. Ishihara, Biomacromolecules 7 (2006) 171–175.
[100] T. Konno, J. Watanabe, K. Ishihara, Biomacromolecules 5 (2004) 342–347.
[101] J. Watanabe, K. Ishihara, Bioconjugate Chem. 18 (2007) 1811–1817.
[102] J. Park, S. Kurosawa, J. Watanabe, K. Ishihara, Anal. Chem. 76 (2004) 2649–2655.
[103] T. Konno, T. Ito, M. Takai, K. Ishihara, J. Biomater. Sci. Polym. Edn. 17 (2006) 1347–1357.
[104] T. Ito, J. Watanabe, M. Takai, T. Konno, Y. Iwasaki, K. Ishihara, Colloids Surf. B: Biointerfaces 50 (2006) 55–60.
[105] X. Wu, H. Liu, J. Liu, K.N. Haley, J.A. Treadway, J.P. Larson, N. Ge, F. Peale, M.P. Bruchez, Nat. Biotechnol. 21 (2003) 41–46.
[106] J.K. Jaiswal, H. Mattoussi, J.M. Mauro, S.M. Simon, Nat. Biotechnol. 21 (2003) 47–51.
[107] S. Pathak, S. Choi, N. Arnheim, M.E. Thompson, J. Am. Chem. Soc. 123 (2001) 4103–4104.

[108] W.J. Parak, R. Boudreau, M. Le Gros, D. Gerion, D. Zanchet, C.M. Micheel, S.C. Williams, A.P. Alivisatos, C. Larabell, Adv. Mater. 14 (2002) 882–885.
[109] I.L. Medintz, A.R. Clapp, H. Mattoussi, E.R. Goldman, B. Fisher, J.M. Mauo, Nat. Mater. 2 (2003) 630–638.
[110] A.R. Clapp, I.L. Medintz, J.M. Mauro, B.R. Fisher, M.G. Bawendi, H. Mattoussi, J. Am. Chem. Soc. 126 (2004) 301–310.
[111] M.E. Akerman, W.C.W. Chan, P. Laakkonen, S.N. Bhatia, E. Ruoslahti, Proc. Natl. Acad. Sci. U.S.A. 99 (2002) 12617–12621.
[112] X. Gao, Y. Cui, R.M. Levenson, L.W.K. Chung, S. Nie, Nat. Biotechnol. 22 (2004) 969–976.
[113] S. Kim, Y.T. Lim, E.G. Soltesz, A.M. De Grand, J. Lee, A. Nakayama, J.A. Parker, T. Mihalijevic, R.G. Laurence, D.M. Dor, L.H. Cohn, M.G. Bawendi, J.V. Frangioni, Nat. Biotechnol. 22 (2004) 93–97.
[114] C.B. Murray, D.J. Norris, M.G. Bawendi, J. Am. Chem. Soc. 115 (1993) 8706–8715.
[115] R. Matsuno, Y. Goto, T. Konno, M. Takai, K. Ishihara, J. Nanosci. Nanotechnol. 9 (2009) 358–365.
[116] Y. Goto, R. Matsuno, T. Konno, M. Takai, K. Ishihara, Biomacromolecules 9 (2008) 3252–3257.
[117] Y. Goto, R. Matsuno, T. Konno, M. Takai, K. Ishihara, Trans. Mater. Res. Soc. Jpn. 34 (2009) 189–192.
[118] K. Masuda, R. Matsuno, T. Konno, M. Takai, K. Ishihara, Trans. Mater. Res. Soc. Jpn. 35 (2010) 147–150.

Dr. Ryosuke Matsuno is an assistant professor in the Department of Materials Engineering, School of Engineering, at the University of Tokyo. He received his Ph.D. degree in engineering from Kyushu University, Japan, in 2006. He was a member of the Center for NanoBio Integration (CNBI), at the University of Tokyo from 2006 to 2010. He is currently a member of the Core Research for Evolutional Science and Technology program (CREST), administered by the Japan Science and Technology Agency (JST). His research is directed to the synthesis of new compounds and well-controlled polymers as well as the evaluation of biointerfacial characteristics and interactions between cellular materials.

Prof. Kazuhiko Ishihara is a professor in the Department of Materials Engineering, Department of Bioengineering, School of Engineering, at the University of Tokyo. He also holds an appointment with the Center for Medical System Innovation (CMSI) at the University of Tokyo. He received his Ph.D. degree from Waseda University in Tokyo in 1984. He began his research career at the Sagami Chemical Research Center in 1984 and then moved to the Tokyo Medical Dental University where he worked from 1987 to 1998. He has been at the University of Tokyo since 1998. His research interests have expanded from polymer science to biomaterials science and engineering, biointerface engineering, and nanobioengineering. He is member of the College of Fellows at the American Institute for Medical and Biological Engineering (AIMBE) and a member of the College of Fellows in the International Union of Biomedical Science and Engineering (IUSBSE). He has received several awards from academic societies as well as industrial organizations.

Colloids and Surfaces B: Biointerfaces 88 (2011) 215–220

Contents lists available at ScienceDirect

Colloids and Surfaces B: Biointerfaces

journal homepage: www.elsevier.com/locate/colsurfb

Effects of 3,4-dihydrophenyl groups in water-soluble phospholipid polymer on stable surface modification of titanium alloy

Ye Yao[a,c], Kyoko Fukazawa[a], Nan Huang[c], Kazuhiko Ishihara[a,b,*]

[a] Department of Materials Engineering, The University of Tokyo, 7-3-1, Hongo, Bunkyo-ku, Tokyo 113-8656, Japan
[b] Department of Bioengineering, The University of Tokyo, 7-3-1, Hongo, Bunkyo-ku, Tokyo 113-8656, Japan
[c] Department of Materials Science and Technology, Southwest Jiaotong University, Chengdu, Sichuan, China

ARTICLE INFO

Article history:
Received 21 April 2011
Accepted 24 June 2011
Available online 18 July 2011

Keywords:
Surface modification
Phospholipid polymer
3,4-dihydroxyphenyl groups
Titanium alloy substrate
Reduced biofouling

ABSTRACT

The surface of a titanium (Ti) alloy substrate was modified by a simple and quick process using a water-soluble polymer, and the effects of 3,4-dihydroxyphenyl (DHP) groups in the polymer side chain on the modification process were examined. The polymers (PMDP) composed of both 2-methacryloyloxyethyl phosphorylcholine (MPC) unit and 3,4-dihydroxyphenyl methacrylate unit were synthesized for surface anchoring. The Ti alloy substrate was coated with PMDP using an aqueous solution of the polymer. A PMDP layer with a thickness of 20 nm was formed on the Ti alloy substrate simply by dip coating for 10 s without drying. Even when the Ti alloy substrate with PMDP coating was immersed in the aqueous medium for 1 week, no change in the thickness was observed, i.e., the PMDP layer was bound to the surface very stably. Oxidation of the DHP groups reduced the stability of the polymer layer significantly. Thus, the DHP groups play a significant role in achieving stable binding. Protein was adsorbed on the Ti alloy substrate; however, this was not observed for the PMDP-coated Ti alloy substrate. In conclusion, we confirmed the effects of DHP groups in PMDP on the stability of the coating on the Ti alloy substrate. Moreover, we found that surface treatment using PMDP was simple, quick, and reliable, and thus, it has great potential for improving biofouling of Ti alloy substrates used in medical devices.

1. Introduction

Titanium (Ti) alloys have many desirable properties such as a relatively low Young's modulus, good fatigue strength, formability, machinability, and corrosion resistance. Accordingly, they have been widely used in biomedical devices and components since the late 1970s, especially in cardiac and cardiovascular applications (e.g., prosthetic heart valves, protective cases in pacemakers, implantable blood pumps, cardiovascular stents, and circulatory devices) [1]. However, Ti alloy substrates induce severe biological responses such as thrombus formation and tissue reaction [2]. As a result, anticoagulant therapy is necessary to minimize the risk of thromboembolic complications. Therefore, surface modification of Ti alloy substrates is indispensable for improving its thrombogenicity and tissue compatibility.

Protein adsorption is the first essential event followed by biological responses such as acute thrombus formation and inflammation and then fibrous encapsulation, bacterial adhesion, and infection [3]. It is generally believed that reducing protein adsorption on the substrates can significantly attenuate these adverse biological responses. One well-known polymeric material used to prevent protein adsorption is hydrophilic poly(ethylene glycol) (PEG) [4]. Indeed, PEG functions well under both in vitro and in vivo conditions for a relatively short period. However, because PEG-based materials are susceptible to degradation by spontaneous oxidation under physiological conditions, these systems lack long-term stability, which reduces their effectiveness as a surface modifier [5]. In other words, PEG-based materials are not suitable for use in implantable cardiovascular devices.

Another promising and effective way of preventing protein adsorption to attain biocompatibility is to prepare an artificial cell membrane surface on the substrates using phospholipid polymers. Such polymers have been synthesized using 2-methacryloyloxyethyl phosphorylcholine (MPC), which is a methacrylate monomer bearing the same polar group as that in the natural phospholipid molecules in the side chain [6,7]. Ishihara et al. developed a synthetic route for MPC in 1989 that has been successfully applied worldwide. MPC polymers show adequate stability both chemically and physically even when under in vivo conditions. Moreover, they have excellent thrombogenicity and tissue

* Corresponding author at: The University of Tokyo, Department of Materials Engineering, 7-3-1, Hongo, Bunkyo-ku, Tokyo, 113-8656, Japan.
Tel.: +81 3 5841 7124; fax: +81 3 5841 8647.
E-mail address: ishihara@mpc.t.u-tokyo.ac.jp (K. Ishihara).

0927-7765/$ – see front matter © 2011 Elsevier B.V. All rights reserved.
doi:10.1016/j.colsurfb.2011.06.034

compatibility [8–12]. At present, MPC polymers are widely used for the surface modification of implantable medical devices and artificial organs [13–17].

There are many reports of surface immobilization of MPC polymers on Ti alloy substrates. However, these methods have many limitations for widespread practical use. Layer-by-layer assembly (LBL) involves complex multistep procedures [18], the self-assembled monolayer (SAMs) technique requires surface-specific interaction [19], and surface-initiated atom transfer radical polymerization (ATRP) needs unstable polymerization conditions [20]. Poly(MPC-co-*n*-butyl methacrylate (BMA)) (PMB) is a typical MPC polymer. The polymer suppresses non-specific protein adsorption, platelet adhesion, activation, and aggregation in whole blood, even in the absence of anticoagulants [8–11,21]. The coating procedure of PMB from its solution is relatively simple [8–10,16]. PMB can be tightly bound to the substrate by the drying process. More than 5 h of prehydration time is needed to enable the surface functionalities of PMB, although the time depends on the thickness of the PMB layer [22]. However, this prehydration process cannot be applied to medical devices such as cardiovascular stents and blood separation devices. Thus, for practical applications, it is desirable to use a more simple, convenient, and versatile method to immobilize MPC on Ti alloy substrate surface without prehydration.

Recently, to facilitate convenient adhesion of organic compounds to metal substrates, mussel-inspired chemistry has been widely investigated [23–25]. Mussels can rapidly and permanently adhere to all types of inorganic and organic wet surfaces in aqueous environments. Such adhesive properties rely on the repeated 3,4-dihydroxy-L-phenylalanine (DOPA) motif found in the foot protein of mussels [26]. Although the exact mechanism of adhesion is not fully understood, it has been widely speculated that the 3,4-dihydroxyphenyl (DHP) group of DOPA is responsible for the adhesion [27,28]. Lee [29] reported that the oxidation of the DOPA motif in the foot proteins dramatically reduces the strength of adhesion to metals. This mussel-inspired chemistry can be used for surface modification using polymers. When a polymer with DHP groups is in contact with a metal substrate, the thin polymer film is spontaneously deposited on the surface. The functionalization of the polymers imparts new characteristics to the metal substrate. In fact, it has been reported that PEG with DHP groups was used to modify a TiO_2 surface in the pH range 6.0–7.4 to reduce protein adsorption on the surface [30].

In this study, we synthesized water-soluble MPC polymers that have DHP groups in the side chain (PMDP). Surface modification of the Ti alloy substrate was carried out using an aqueous solution of the polymer. The surface characteristics and stability of the coated polymer layer were examined, and the effects of the DHP groups on the adhesion of PMDP have been discussed. Finally, we examined the reduction of protein adsorption on the surface of the Ti alloy substrate after modification using PMDP.

2. Materials and methods

2.1. Materials

Two types of water-soluble MPC polymer, poly(MPC-co-methacrylic acid (MAA)) (PMA), were obtained from NOF Co. (Tokyo, Japan) which were synthesized by conventional radical polymerization of MPC and MAA [31]. The compositions of the MPC units in PMA were 30 unit mol% (denoted PMA3) and 50 unit mol% (denoted PMA5). The number average molecular weight (Mn) of PMA3 and PMA5 was 2.7×10^5 and 3.2×10^5, respectively. Dopamine hydrochloride was purchased from Sigma–Aldrich (St. Louis, MO, USA). 1-Ethyl-3-(3-dimethylaminopropyl)carbodiimide, hydrochloride (WSC) was purchased from Dojindo (Kumamoto, Japan). A Ti alloy substrate with thickness of 1.0 mm was purchased from Sumitomo Metals, Ltd. (Tokyo, Japan). The Ti alloy substrate was cut into 10 mm × 10 mm pieces and polished with #2000 and #3000 polish papers. The pieces were then rinsed in acetone and ethanol by sonication for 15 min. After drying in air, the substrates were cleaned using oxygen plasma apparatus (PR500 plasma reactor, Yamato Science, Tokyo, Japan) for 10 min before use. To test the resistance of the substrate surface to protein adsorption, bovine serum albumin (BSA, Sigma–Aldrich) was used without further purification.

2.2. Synthesis of phospholipid polymer

The water-soluble MPC polymer with DHP groups was synthesized by condensation reaction between PMA and dopamine hydrochloride. The reaction scheme is shown in Fig. 1. Dopamine hydrochloride and WSC were dissolved in 4 mL of PMA aqueous solution (5.0 wt%), and 96 mL of pH 6.0 buffered solution (potassium dihydrogen phosphate and sodium hydroxide) was added. The reaction was carried out at room temperature for 24 h under Ar gas atmosphere to prevent the oxidation of the DHP groups. The molar ratio [dopamine hydrochloride]/[COOH] was 2.0. After the reaction, the polymer solution was filtered using ultrafiltration membranes (Millipore Co., USA; molecular size cut off: 3.0×10^4) until there was no further release of unreacted dopamine through the membrane, which was confirmed by ultraviolet (UV, V-560, Jasco Co., Tokyo, Japan) adsorption. The polymer solution was freeze-dried. PMDP prepared from PMA3 are denoted as PMDP3, and that prepared from PMA5 are denoted as PMDP5. The chemical structure of these polymers was confirmed by both UV and Fourier transform infrared (FTIR) spectroscopy (FT/IR-615, Jasco) for 32 scans over the range 650–4000 cm^{-1} at a resolution of 4.0 cm^{-1}. The contents of the DHP groups in PMDP were calculated from the UV absorbance of the polymer aqueous solution at 280 nm by comparing with that of a given concentration of dopamine hydrochloride.

2.3. Surface modification on Ti alloy substrate with PMDP

The PMDP solution was prepared using the following aqueous media: pure water (pH about 5.5) and buffered solutions with pH 6.0 and 8.5. The Ti alloy substrate was coated with the PMDE solution by simply dipping it in the solution at room temperature for either 10 s or 24 h.

The surface of the substrate was analyzed by FTIR reflection adsorption spectroscopy to confirm that the substrate coated with the solution. The surface morphology was then observed using an atomic force microscope (AFM, Nihon Veeco, Tokyo, Japan) operated in the tapping mode. The measurements were performed under ambient conditions using a standard cantilever at a scan rate of 1.0 Hz. The root mean square (RMS) surface roughness was calculated from the roughness profiles.

Following the polymer adhesion process, a quartz crystal microbalance (QCM) sensor was used with dissipation monitoring (QCM-D, Q-Sense, Gothenburg, Sweden) and a fundamental resonant frequency of 5.0 MHz. The QCM is widely used to measure the change in mass (Δm) of materials/molecules attached to the surface of the QCM sensor via changes in the resonant frequency (Δf). The QCM-D can detect adsorbed mass up to a resolution of less than a few nanograms per square centimeter. The resonant frequency of the QCM sensor (f) depends on the total oscillating mass. When a thin film is attached to the QCM sensor, the frequency decreases; if the film is thin and rigid, the decrease in frequency is proportional to the mass of the film. Thus, the amount of the adsorbed material on a given surface can be measured by the decrease in the frequency of the oscillator. In this manner, the QCM operates as a very sensitive balance. The mass of the adhered layer can be calcu-

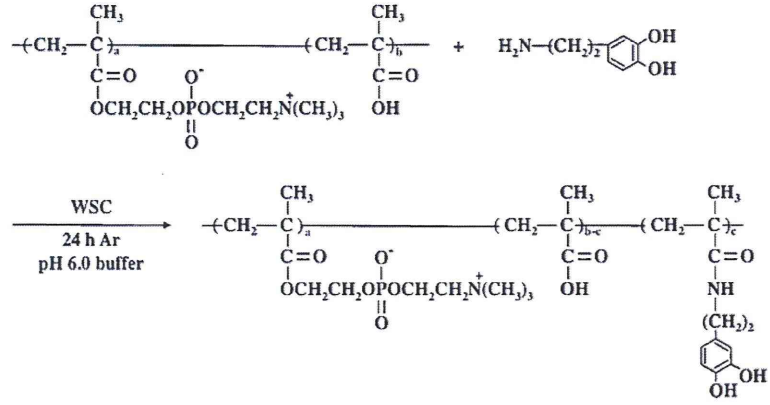

Fig. 1. Synthetic route of PMDP.

lated using the Sauerbrey equation [32], $\Delta m = -C \times \Delta fn/n$, where $C = 17.7\ \mathrm{ng\,cm^{-2}\,Hz^{-1}}$, n is the overtone number ($n = 1, 3, 5, 7.$), and fn is the frequency of the overtone. Four resonant frequencies (overtones, $n = 1$, 3, 5, and 7) were used to detect the oscillation of the shearwave through the crystal at 5, 15, 25, and 35 MHz, respectively. The data from the seventh overtone is reported, because it contained minimum noise. The Ti-coated (Ti/Au) QCM sensor obtained from Q-Sense was cleaned using oxygen plasma for 10 min before use. The QCM sensor was exposed to the water solution until a stable baseline of the QCM signals was obtained. The QCM cell was then filled with 2.0 mg mL^{-1} of PMDP aqueous solution. After the PMDP solution was retained for 20 min in the QCM cell, phosphate buffered saline (PBS) solution was flowed to replace the PMDP solution and wash away the weakly adsorbed PMDP from the surface. The QCM signals were monitored throughout the procedure. All the measurements were performed at 37 °C and repeated at least three times.

2.4. Surface characterization and stability evaluation of the coating polymer layer

After coating, the Ti alloy substrates were immersed in water at room temperature for at least 2 days to evaluate the stability of the coating polymer layer. The hydrophilicity of the Ti alloy substrates before and after immersion in the PMDP solution was evaluated with a contact angle goniometer (CA-W, Kyowa Co. Ltd., Tokyo, Japan). The captive-bubble method was used to determine the static contact angle. Each Ti alloy substrate was immersed in water to equilibrate and then fixed horizontally on a metal plate. A small air bubble was attached to the surface of the Ti alloy substrates. The measurement was repeated five times for each substrate, and the average was calculated.

The thickness of the PMDP layer formed on the substrate was measured using an ellipsometer (J. A. Woollam Co., Inc., Tokyo, Japan) at an incident angle of 70° in the visible region. The thickness of the polymer coating layer was determined using a Cauchy layer model with an assumed refractive index of 1.49 at 632.8 nm.

A surface elemental analysis was carried out using an X-ray photoelectron spectroscope (XPS, AXIS-HSi165, Kratos/Shimadzu Co., Kyoto, Japan) with 15 kV Al Kα radiation source at the anode. The applied voltage was 15 kV, and the electric current was 10 mA. The take-off angle of the photoelectrons was maintained at 90°.

To examine the effects of oxidation of the DHP groups in PMDP, the PMDP aqueous solution was kept in air for spontaneous oxidization. After one month, the solution was freeze-dried, and the chemical structure of the remaining polymer was analyzed by both UV and FTIR spectroscopy. The polymer was dissolved in water again, and the solution was used for coating the Ti alloy substrate. The stability of the polymer layer was evaluated by ellipsometry.

2.5. Measurement of amount of protein adsorbed on Ti alloy substrate

The amount of BSA adsorbed on the PMDP3-coated surface was quantified using the QCM-D. First, a Ti-coated QCM sensor was used as a QCM-D. After flowing 2.0 mg mL^{-1} of PMDP3 aqueous solution through the QCM cell, the sensor was exposed to a PBS (pH 7.4) solution until a stable baseline of QCM signals was obtained. Then, 1.0 mg mL^{-1} of BSA in PBS was flowed to fill the QCM cell. After the BSA solution was retained for 20 min in the QCM cell, the PBS solution was flowed to replace the BSA solution and wash away the weakly adsorbed BSA from the surface. The QCM signals were monitored throughout the procedure. All the measurements were performed at 37 °C and repeated at least three times.

3. Results and discussion

3.1. Characterization of PMDP

We considered that the DHP groups were useful for binding the polymer after adsorption on the Ti alloy substrate from its aqueous solution. The IR spectra of the two PMDP polymers are shown in Fig. 2 with the starting materials, PMA and dopamine hydrochloride. The IR spectra of PMDP3 and PMDP5 were similar. The DHP group in PMDP was verified by the appearance of an absorbance

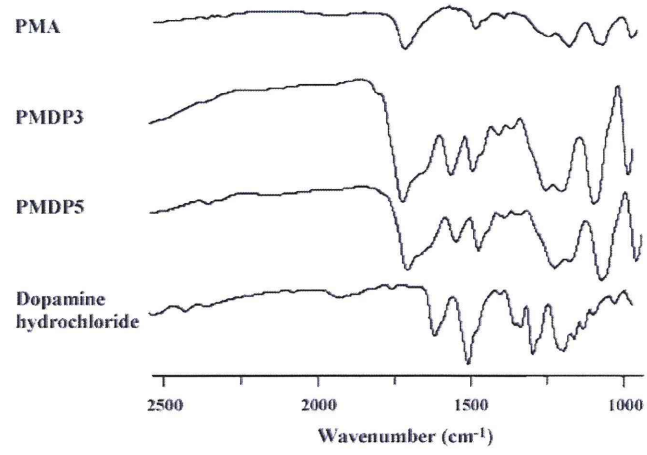

Fig. 2. IR spectra of PMA, PMDP, and dopamine hydrochloride.

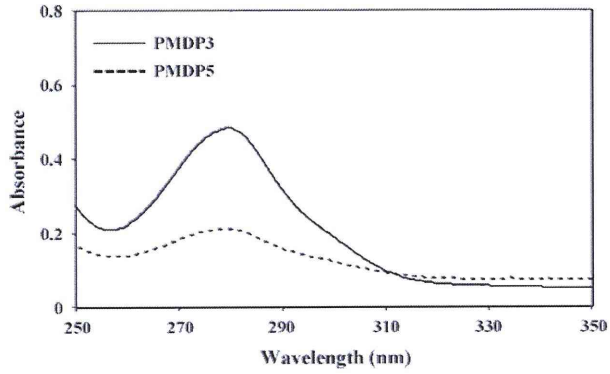

Fig. 3. UV absorption spectrum of PMDP aqueous solution (only the spectrum of PMDP3 is shown).

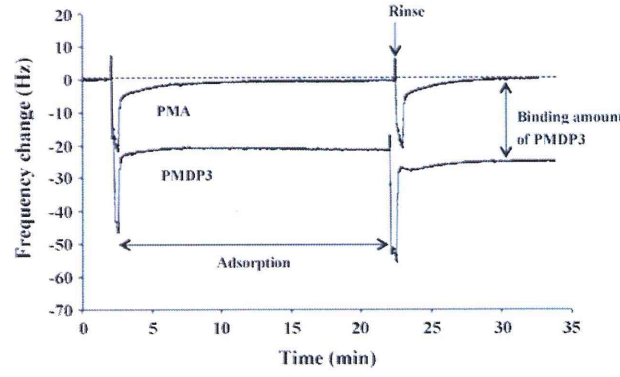

Fig. 5. Adsorption and binding process of PMDP3 and PMA3 on Ti-coated QCM sensor.

peak at 1553 cm^{-1}, which is attributed to the aromatic ring of dopamine hydrochloride. In addition, the presence of the ester carbonyl group of the methacrylate units in PMDP was verified by the appearance of an absorbance peak at 1715 cm^{-1}. The UV spectrum shown in Fig. 3 confirms the introduction of the DHP group in PMDP. An adsorption was observed at 280 nm, corresponding to the DHP groups. Absorbance calculations showed that the content of DHP groups was 4.0 unit mol% in PMDP3 and 2.0 unit mol% in PMDP5. The content of DHP groups in the polymer chain was less than expected. This was because of the solubility of dopamine hydrochloride and reactivity of carboxylate groups in PMA at this pH.

3.2. Surface modification on Ti alloy substrate with PMDP

The Ti alloy substrate was immersed in the aqueous solution of PMDP for different periods. After immersion in the PMDP solution for 10 s, the Ti alloy substrate was pulled out and dried under vacuum for observation with AFM. The AFM images are shown in Fig. 4. The RMS surface roughness of the original Ti alloy substrate was 1.0 nm, whereas that of the PMDP3-coated Ti alloy substrate was only 0.5 nm, indicating that the surface roughness can be reduced by this polymer coating process. The amount of polymer on the Ti alloy substrate was measured with QCM-D. As shown in Fig. 5, a small amount of PMA was deposited on the substrate (small change in frequency); on the other hand, 354 ng cm^{-2} of PMDP3 adhered to the substrate (20 Hz change in frequency). These results show that PMDP3 covered and adhered to the Ti alloy substrate immediately

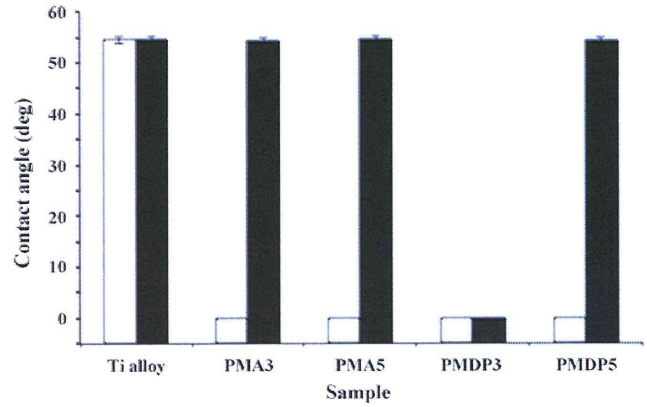

Fig. 6. Change in contact angle of Ti alloy substrate treated with PMA and PMDP by immersion in water for 2 days. Open column: Just after coating for 10 s. Closed column: After 2 days.

from its aqueous solution and formed a uniform coating layer via the dipping procedure. The peaks of DHP groups in the FTIR spectra also indicate the presence of PMDP3 on the Ti alloy substrate and ester carbonyl group after the coating procedure (data not shown).

The surface hydrophilicity was evaluated by performing contact angle measurements. PMDP is water-soluble, which means the polymer is quite hydrophilic. The contact angle was 54° on the original Ti alloy substrate, as shown in Fig. 6. After treatment

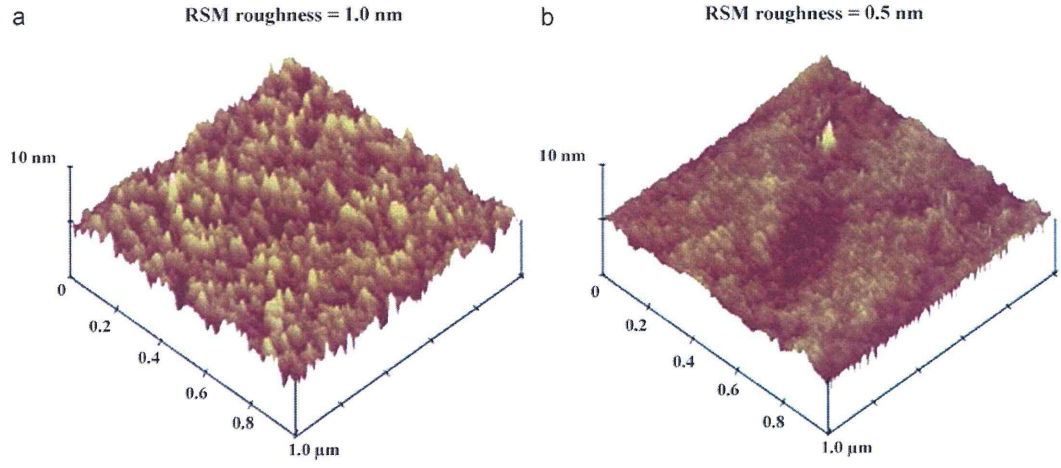

Fig. 4. AFM images of (a) original Ti alloy substrate and (b) Ti alloy substrate coated with PMDP3 by immersion for 10 s.

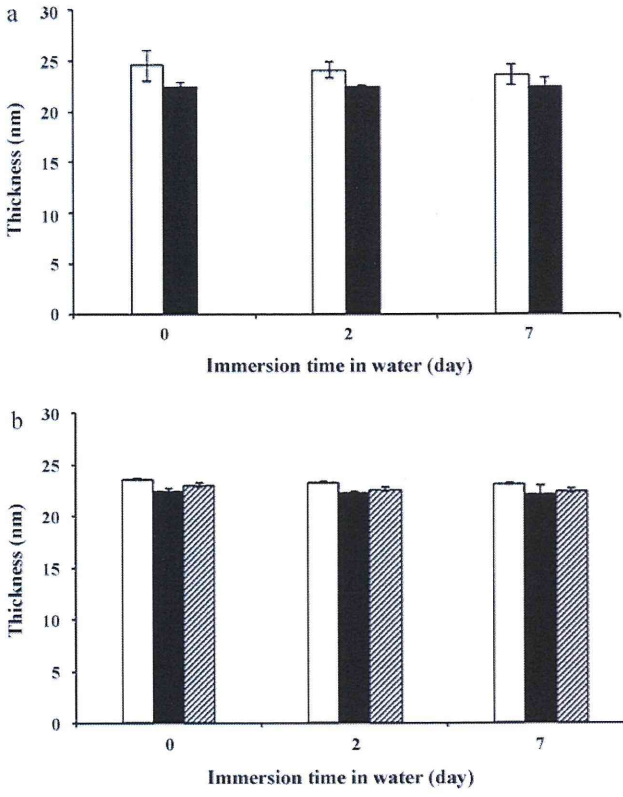

Fig. 7. Change in thickness of PMDP3 layer on Ti alloy substrate after immersion in water. (a) For different coating times (open column: 24 h; closed column: 10 s) and (b) with different pH (open column: pH 8.5 buffer; closed column: water; hatched column: pH 6.0 buffer).

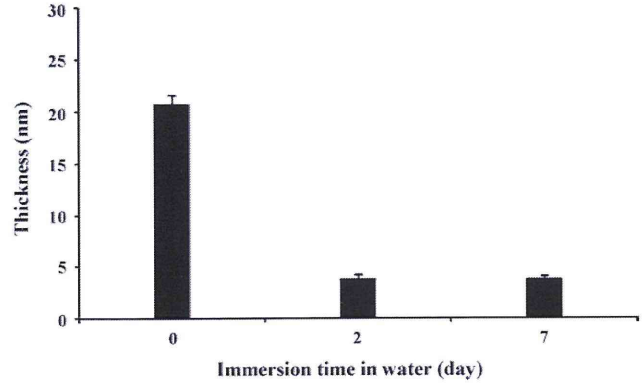

Fig. 8. Change in thickness of oxidized PMDP3 layer on Ti alloy substrate after immersion in water.

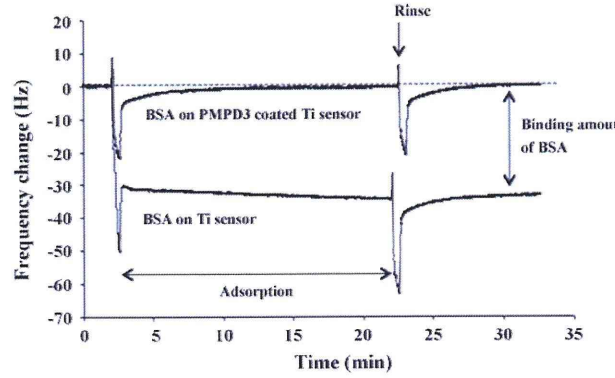

Fig. 9. Adsorption and detachment process of BSA on bare and PMDP3-modified Ti-coated QCM sensor.

with the PMDP3 solution, the contact angle decreased dramatically and reached 0°. This value was maintained even after the substrate was immersed in water for 2 days. This result suggests that PMDP3 remained on the substrate. On the other hand, in the case of PMA and PMDP5, the contact angle returned to 54° (the same as in the case of the original Ti alloy substrate) after immersion for 2 days. These polymers may be detached from the substrate. As shown in Fig. 7, the stability of the PMDP3 coating was confirmed by ellipsometry from the thickness change observed during the washing process. For both time periods (10 s and 24 h), in the case of the PMDP3 aqueous solution, the thickness of the coating layer did not change and minor differences because of the different coating periods and pH were observed. The signals of phosphorus atom at 133 eV and carbon atoms at 285–288 eV in the XPS spectra support the presence of PMDP on the Ti alloy substrate after 7 days immersion procedure (data not shown). Although the binding mechanism of the DHP group to the metal and metal oxide could not be clarified, the affinity of the DHP groups to the Ti alloy substrate was observed.

On the other hand, we considered that the reduced content of DHP groups because of oxidation may lead to instability of the polymer layer. The PMDP aqueous solution was spontaneously oxidized by air. Then, the chemical composition was studied by UV and FTIR spectroscopy. In the UV spectrum measured after oxidation, the intensity of the absorbance peak at 280 nm attributed to the aromatic ring decreased. Conversely, an IR absorbance peak appeared at 2852 cm^{-1}; this is attributed to ketone groups. The above results confirm that the DHP groups were converted to quinine groups. The oxidized PMDP solution was used as a coating solution. As shown in Fig. 8, the thickness of the coating polymer layer changed with the washing period, and the thickness decreased within 2 days. Thus, the oxidation reaction weakened the binding force of the polymer on the Ti alloy substrate and caused the coating polymer layer to become unstable. These results strongly support the notion that the DHP groups in PMDP play an important role in stabilizing the coating.

3.3. *Protein adsorption resistance of Ti alloy substrate treated with PMDP*

Resistance to protein adsorption is one of the most important properties of biomedical materials. The effects of coating with PMDP3 were evaluated using the BSA solution. BSA is the most highly concentrated protein in blood plasma. According to the QCM signals (Fig. 9), 530 ng cm^{-2} of BSA was adsorbed on the original Ti alloy substrate (30 Hz change in frequency), whereas after treatment with PMDP3, no QCM signal because of BSA adsorption could be detected. These results indicate that the resistance to protein adsorption can be improved by coating with PMDP3. The MPC polymer gave a phosphorylcholine-group-arranged surface [22,33]. The phosphorylcholine group is electrically neutral and hydrated with free-water-like water molecules [11,34,35]. Thus, both electrostatic interaction and hydrophobic interaction are extremely weak and resistance to protein adsorption on the surface is improved [36].

4. Conclusions

A uniform layer of PMDP3 can be deposited on a Ti alloy substrate simply by dipping for 10 s in a PMDP3 aqueous solution without further treatment. The DHP groups play an important role as molecular anchors for stabilizing the binding between the coat-

ing and the substrate. The reduction of protein adsorption on the surface treated with PMDP may induce significant suppression of biological responses, thus maintaining excellent biocompatibility of the MPC unit. In conclusion, simple and reliable surface treatment of a Ti alloy substrate was successfully carried out using bioinspired PMDP, and this method has the potential for application to high-performance cardiovascular implantable medical devices.

Acknowledgement

The authors thank Prof. Madoka Takai, Dr. Yuuki Inoue, and Dr. Ryosuke Matsuno from The University of Tokyo for the helpful discussions. This research was conducted under the CSC program in China at The University of Tokyo. One of the authors (YY) expresses her gratitude. The research was partially supported by Core Research for Evolutional Science and Technology (CREST), Japan Science and Technology Agency.

References

[1] X. Liu, P.K. Chu, C. Ding, Mater. Sci. Eng. R. 47 (2004) 49.
[2] J. Hong, J. Andersson, K. Ekdahl, et al., Thromb. Haemost. 82 (1999) 58.
[3] D.G. Castner, B.D. Ratner, Surf. Sci. 500 (2002) 28.
[4] C. Gao, G. Li, H. Xue, et al., Biomaterials 31 (2010) 1486.
[5] C.W. Mcgary Jr., J. Polym. Sci. 46 (1960) 51.
[6] K. Ishihara, T. Ueda, N. Nakabayashi, Polym. J. 22 (1990) 355.
[7] T. Ueda, H. Oshida, K. Kurita, et al., Polym. J. 24 (1992) 1259.
[8] K. Ishihara, R. Aragaki, T. Ueda, et al., J. Biomed. Mater. Res. 24 (1990) 1069.
[9] K. Ishihara, N.P. Ziats, B.P. Tierney, et al., J. Biomed. Mater. Res. 25 (1991) 1397.
[10] K. Ishihara, H. Oshida, T. Ueda, et al., J. Biomed. Mater. Res. 26 (1992) 1543.
[11] K. Ishihara, H. Nomura, T. Mihara, et al., J. Biomed. Mater. Res. 39 (1998) 323.
[12] A.L. Lewis, Colloids Surf. B: Biointerfaces 18 (2000) 261.
[13] T. Yoneyama, K. Ishihara, N. Nakabayashi, et al., J. Biomed. Mater. Res. 43 (1998) 15.
[14] A.L. Lewis, L.A. Tolhurst, P.W. Stratford, Biomaterials 23 (2002) 1697.
[15] M. Galli, L. Sommariva, F. Prati, et al., Catheter. Cardiovasc. Intervent. 53 (2001) 182.
[16] T.A. Snyder, H. Tsukui, S.I. Kihara, et al., J. Biomed. Mater. Res. Part A 81A (2007) 85.
[17] T. Moro, Y. Takatori, K. Ishihara, et al., Nat. Mater. 3 (2004) 829.
[18] J. Choi, T. Konno, T. Matsuno, et al., Colloids Surf. B: Biointerfaces 67 (2008) 216.
[19] Y. Iwasaki, N. Saito, Colloids Surf. B: Biointerfaces 32 (2003) 77.
[20] Y. Zhao, Q. Tu, J. Wang, et al., Appl. Surf. Sci. 257 (2010) 1596.
[21] Y. Iwasaki, K. Ishihara, Anal. Bioanal. Chem. 381 (2005) 534.
[22] A. Yamasaki, Y. Imamura, K. Kurita, Colloid Surf. B: Biointerfaces 28 (2003) 53.
[23] H. Lee, S. Dellatore, W. Miller, et al., Science 318 (2007) 426.
[24] K. Huang, B.P. Lee, D.R. Ingram, et al., Biomacromolecules 3 (2002) 397.
[25] H. Lee, S.M. Dellatore, W.M. Miller, et al., Science 318 (2007) 426.
[26] J.H. Waite, M.L. Tanzer, Science 212 (1981) 1038.
[27] A.A. Ooka, R.L. Garrell, Biopolymers 57 (2000) 92.
[28] M. Yu, J. Hwang, T.J. Deming, et al., J. Am. Chem. Soc. 121 (1999) 5825.
[29] H. Lee, N.F. Scherer, P.B. Messersmith, et al., Proc. Nat. Am. Sci. U.S.A. 103 (2006) 12999.
[30] J.L. Dalsin, L. Lin, S. Tosatti, et al., Langmuir 21 (2005) 640.
[31] M. Kimura, K. Fukumoto, J. Watanabe, et al., J. Biomater. Sci. Polym. Ed. 15 (2004) 631.
[32] G. Sauerbrey, Z. Phys, A: Hadrons Nucl. 155 (1959) 206.
[33] S. Clarke, M.C. Davies, C.J. Roberts, et al., Langmuir 16 (2000) 5116.
[34] H. Kitano, K. Sudo, K. Ichikawa, et al., J. Phys. Chem. B 104 (2000) 10425.
[35] H. Kitano, M. Imai, T. Mori, et al., Langmuir 19 (2003) 10260.
[36] Y. Xu, M. Takai, K. Ishihara, Ann. Biomed. Eng. 38 (2010) 1938.

Tribology International 46 (2012) 225–236

Contents lists available at ScienceDirect

Tribology International

journal homepage: www.elsevier.com/locate/triboint

Analysis of biphasic lubrication of articular cartilage loaded by cylindrical indenter

Nobuo Sakai [a,*], Yuichiro Hagihara [a], Tsukasa Furusawa [a], Natsuko Hosoda [b], Yoshinori Sawae [a], Teruo Murakami [a]

[a] Department of Mechanical Engineering, Kyushu University, 744 Motooka, Nishi-ku, Fukuoka 819-0395, Japan
[b] Former Kyushu University, Japan

ARTICLE INFO

Article history:
Received 4 September 2010
Received in revised form
30 December 2010
Accepted 18 March 2011
Available online 8 April 2011

Keywords:
Articular cartilage
Biphasic lubrication
Finite element
Migrating contact

ABSTRACT

Combination of theoretical biphasic analyses and corresponding experimental measurements for articular cartilage has successfully revealed the fundamental material properties and time-depending mechanical behaviors of articular cartilage containing plenty of water. The insight of load partitioning between solid and fluid phases advanced the prediction of the frictional behavior of articular cartilage. One of the recent concerns about biphasic finite element (FE) analysis seems to be a dynamic and physiological condition in terms of mechanical functionality as a load-bearing for articular joint system beyond material testing, which has mainly focused on time-dependent reaction force and deformation in relatively small and low speed compression. Recently, the biphasic FE model for reciprocating sliding motion was applied to confirm the frictional effect on the migrating contact area. The results indicated that the model of a cylindrical indenter sliding over the cartilage surface remarkably sustained the higher proportion of fluid load support than a condition without migrating contact area, but the effectiveness of constitutive material properties has not been sufficiently evaluated for sliding motion. In our present study, at the first stage, the compressive response of the articular cartilage was examined by high precision testing machine. Material properties for the biphasic FE model, which included inhomogeneous apparent Young's modulus of solid phase along depth, strain-dependent permeability and collagen reinforcement in tensile strain, were estimated in cylindrical indentation tests by the curve fitting between the experimental time-dependent behavior and FE model simulation. Then, the biphasic lubrication mechanism of the articular cartilage including migrating contact area was simulated to elucidate functionality as a load-bearing material. The results showed that the compaction effect on permeability of solid phase was functional particularly in the condition without the migrating contact area, whereas in sliding condition the compaction effect did not clearly show its role in terms of the proportion of fluid load support. The reinforcement of solid phase, which represented the collagen network in the tissue, improved the proportion of fluid load support especially in the sliding condition. Thus, a functional integration of constitutive mechanical properties as a load-bearing was evaluated by FE model simulation in this study.

1. Introduction

Articular cartilage is a superior load-bearing material of diarthrodial joint in endoskeleton bodies. The cartilage layer covers bones in synovial joint to realize excellent frictional properties of prevailing over various rubbing circumstances and loads. The cartilage as a tribological material is exposed to a wide range of loads up to 10 times body weight, while relative speed between rubbing surfaces that includes rolling and sliding motions subsides nearly stationary in activities of daily living. Upon these severe conditions, friction coefficient of synovial joint is maintained within a very low value, which normally ranges under 0.03. In normal body, frictional function of articular cartilage endures through whole life accompanying metabolic regeneration of the cartilaginous tissue. Constitution and functionality of articular cartilage complex as the biphasic lubrication material has been recently reviewed by Ateshian [1] with a conclusive statement. Katta et al. [2] presented the biotribological characteristics of articular cartilage from the viewpoint of various phenomena, which included boundary lubrication and artificial substitutions for the cartilage. In this paper, only a brief introduction of researches on mechanical functionalities of

* Corresponding author. Tel.: +81 92 802 3076; fax: +81 92 802 0001.
E-mail addresses: sakai.nobuo.570@m.kyushu-u.ac.jp, sakai.nobuo@ise.kyutech.ac.jp (N. Sakai), sawa@mech.kyushu-u.ac.jp (Y. Sawae), tmura@mech.kyushu-u.ac.jp (T. Murakami).

0301-679X/$ - see front matter © 2011 Elsevier Ltd. All rights reserved.
doi:10.1016/j.triboint.2011.03.016

articular cartilage is mentioned with sincerely devolving further descriptions on other review papers.

Articular cartilage is a soft tissue containing high water content (70–80% by weight) in an intact state. The high water content is derived from aggregate proteoglycan, which induces osmotic pressure for swelling behavior. Constitutive proteoglycan in the matrix is enmeshed and bound in a fibril network of type II collagen that also functionally reinforces total cartilaginous matrix. The fibril network resists tensile loads in the stress field of the matrix, while proteoglycan (and other quantitative constituents including chondrocyte) mainly takes in charge of supporting compressive load at equilibrium condition. Experimentally, tensile stiffness of articular cartilage is much higher than compressive stiffness of equilibrium condition [3]. Articular cartilage tissue exhibits tension–compression nonlinearity [4,5]. Note that surface constitutions of articular cartilage including gel-like layer, molecular structure on surface and its interaction with synovial fluid lubricants are also employed to enhance reduction of friction force in consideration of boundary lubrication phenomenon [6–11].

It is known that articular cartilage has a constitutive inhomogeneity [12–16] and anisotropy [17,18] form surface to bottom zone. Articular cartilage is briefly divided into 3 characteristic layers along depth direction, whose are called superficial, middle and deep zones. In superficial layer, collagen fibril predominantly lies in parallel to surface plane and concentration of proteoglycan content is lowest within 3 zones. As moving toward middle zone, orientation of collagen fibril tends to be vertical to the surface plane and proteoglycan content rises. In deep zone, collagen fibril is predominantly oriented to vertical to the plane of subchondral bone and proteoglycan content is maintained its concentration as high as that in middle zone. Most bottom of cartilaginous tissue is connected to subchondral bone, called tidemark. Any other constitutive properties of the matrix, which includes density and structure of collagen network, water content, electrical charge, morphology of the cells, etc., vary along depth direction. Consequently, mechanical properties, which are represented as tensile and compressive modulus, permeability of interstitial fluid and so on, also vary along depth direction.

A role of soft material for transmitting loads between articular surfaces is to distribute contact load and consequently reduce the subchondral peak stress. In concerning with articular cartilage, one of the most notable findings on tribological behavior is addressed to the biphasic lubrication mechanism. A fundamental theoretical model of biphasic theory [19] for representing articular cartilage consists of solid phase and fluid phase as a porous media model. When a counter surface contacts to biphasic matrix with some apparent contact area, the fluid content in the tissue is trapped within contact area. Under a load given by counter surface, the collagen network resists interstitial fluid pressure in aggregate solid matrix, and still interstitial fluid cannot flow well in the biphasic matrix due to its low permeability. Then, considerable high pressurization of interstitial fluid occurs under the contact area even in unconfined compression [20]. Thus, the interstitial fluid pressure supports considerable proportion of total load in contact area and this situation consequently causes a reduction of contact force of solid phase. Under an assumption that nonviscous property of fluid phase does not produce friction force, the reduction of the proportion of total contact force on solid phase as a load sharing mechanism subsequently results in low friction coefficient [21]. The biphasic lubrication mechanism has successfully proven the low friction coefficient and time-dependent behavior of articular cartilage by both experimental and theoretical examination past a few decades. Particularly, computational implement for finite element method of biphasic theory advanced predictions of the behavior of cartilaginous tissue including interstitial fluid pressurization. A linear correlation between interstitial fluid pressurization and resultant behavior on friction coefficient, which had been predicted by theoretical analysis [22], was experimentally confirmed with directly utilizing micro pressure sensing device [23].

Combination of theoretical analyses and corresponding experimental measurements has successfully revealed the important material properties of articular cartilage from the viewpoint of biphasic framework. While more detailed expressions of the constitutions of cartilaginous tissue on theoretical model have advanced to obtain more exact behavior [24–34], one of the recent concerns seems to be a dynamic and physiological condition in terms of mechanical functionality as a load-bearing for articular joint system beyond material testing, which is often conducted in relatively smaller loading speed and magnitude than physiological one. In human body, articular cartilage of lower extremity in walking condition is normally exposed to a cyclic load of several times body weight with rolling and sliding motions. Upon considering these conditions, physiological load levels and contact geometries (conformity of two surfaces) were examined in accounting for the shape of hip and/or knee joint in order to interpret a results from material testing level [35,36]. Compressive reaction force of articular cartilage under physiological cyclic loading was experimentally characterized on frequency response [37]. The effect of physiological cyclic loading on experimental frictional response was examined to test whether a cyclic load maintained the interstitial fluid pressure or not, which offers low friction coefficient [38]. The effect of the soft biphasic amorphous layer on the top surface of cartilaginous tissue was verified by the biphasic finite-element (FE) model under cyclic loadings including the physiological frequency [39]. The mechanical role of the deep vertical fibril was found on the reactional stiffness of spherical indentation especially in the transient period of the physiological condition [40].

One of the tribological factors for a load-bearing is to introduce the sliding motion. By experimental friction tests, Caligaris reported that migrating contact area, which delivers re-swelling periods to the tissue, significantly promoted the sustainability of the interstitial fluid pressurization mechanism and consequent low friction coefficient [41]. Also, Pawaskar introduced the sliding motion into a biphasic FE model and remarked the importance of migrating contact area for sustainability of the biphasic lubrication [42], but the effectiveness of complicated material properties has not been sufficiently evaluated for sliding motion. We thought that physiological loading speed and migrating contact area should be important factors for an integration of mechanical properties of articular cartilage to recognize functionality in actual conditions as a load-bearing in living body. In our present study, the compressive response of the articular cartilage in relatively physiological condition was examined by high precision testing machine with a feedback-controlled servomotor. Material properties of biphasic FE model, which included inhomogeneous apparent Young's modulus of solid phase along depth, strain-dependent permeability and collagen reinforcement in tensile strain, were estimated in cylindrical indentation geometry by a curve fitting between the experimental time-dependent behavior and FE model simulation. Then, by using the modulated FE model, the biphasic lubrication mechanism of articular cartilage including migrating contact area was simulated to elucidate functionality as a load-bearing material.

2. Methods

Both experimental material testing and biphasic FE model analysis were conducted mutually to confirm a part of results. In experimental compressive test, relatively high compressive speeds

with large compressive amplitudes were applied to the tissue to observe the dynamic response for expectantly aiming at more physiological condition. The depth-dependent apparent Young's modulus was experimentally obtained from local strain field at equilibrium state. A cylindrical indenter was adopted in both the experimental compression test and FE analysis to examine the effect of sliding motion of the indenter over cartilage surface. Time-dependent compressive response by cylindrical indenter was used to identify the material properties for consequent FE model analysis. In the FE model analysis with sliding indenter, the effect of migrating contact area was examined with more actual material properties for expressing articulation of cartilaginous tissue.

2.1. Experimental apparatus and materials

The compressive test of cartilaginous tissue has been thought in the past to be difficult to gain accurate results in physiological high-speed compression. In this study a self-made compressive tester shown in Fig. 1 was developed to offer precise motion of compressive platen or indenter. The platen was driven by a ball screw (KR-15, THK) and a servomotor (MR-J2-Jr, Mitsubishi Electronic Corporation) via a load cell (LUR-A-50NSA1, Kyowa electronic instruments). Since a load cell involves its own deformation, which disturbs an accuracy of the position of an end effector, the position of the compressive platen was directly detected by Eddy current displacement sensor (E2CA-X1R5A, Omron). A feedback control with the displacement sensor precisely actuated the platen with positional accuracy of 0.5 μm and maximum speed of 4000 μm/s in any loading condition. Sampling rate of overall control loop with a measurement of reaction force was arranged at 333 Hz. The compressive tester was installed on the stage of confocal laser scanning microscope (CLSM, C1-Plus, Nikon Corporation) to observe local strain of the tissue through a glass plate. Both of the compressive platens were made of impermeable alumina ceramics. In compressive test of the cylindrical indenter, additional cylindrical stainless steel with 5 mm radius (SUS316L, impermeable solid) was attached on one of the plate.

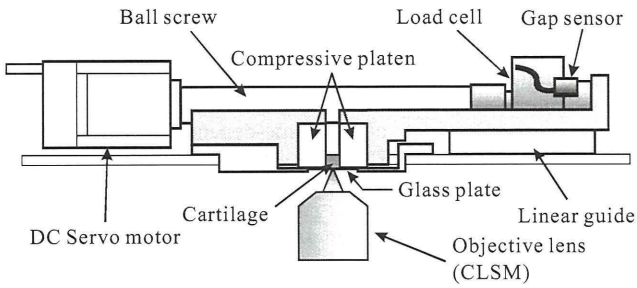

Fig. 1. A schematic drawing of compressive tester for CLSM observation. A feedback control with the displacement sensor (gap sensor using Eddy current) precisely actuated the platen with the position accuracy of 0.5 μm and the maximum speed of 4000 μm/s in any loading condition. The compressive tester was installed on the stage of the CLSM to observe the local strain of the tissue through the glass plate.

Experimental tissue was dissected from distal end of femur in porcine knee (6–8 months old) without any freezing after a processing to prevent change on mechanical properties [43]. For first compressive test on the measurement of depth-dependent strain distribution, a 3 mm cylindrical core with subchondral bone was harvested by a biopsy punch and then split into the half perpendicular to articular surface with a scalpel blade, shown in Fig. 2(a). For the indentation by the cylindrical indenter, a bar shaped osteochondral explant with the dimension of about 2.5 mm width and 10 mm length was dissected by a scalpel blade with preserving intact surface of the tissue, shown in Fig. 2(b). The direction of the longitudinal axis of the bar explant was parallel to physiological anterior–posterior line in the chondyle. The samples were washed by PBS (Phosphate Buffered Saline; pH 7.4, Invitrogen Corporation). Then, living cells as markers for recognizing deformation of solid phase were stained with Calcein-AM (C-3099, Molecular Probes.). The samples were incubated for 30 min staining and washed by PBS again. Compressive tests were examined in PBS solution through the experiment to maintain moisture of the tissue and osmotic phenomenon.

For the compressive test, osteochondral specimen was put on the glass plate and compressed in a condition of unconfined compression. Since the entire specimen in our experiment preserved subchondral bone, the depth of each cartilaginous tissue was acquired prior to the test by measuring the image length from surface to tidemark in microscopic view. Before the compressive test, initial compressive load with 0.05 N of peak load was given for 5 s to make sure of a stable contact. Then, the initial load was removed and the compressive test was immediately executed under the observation of microscopic view. The cartilage

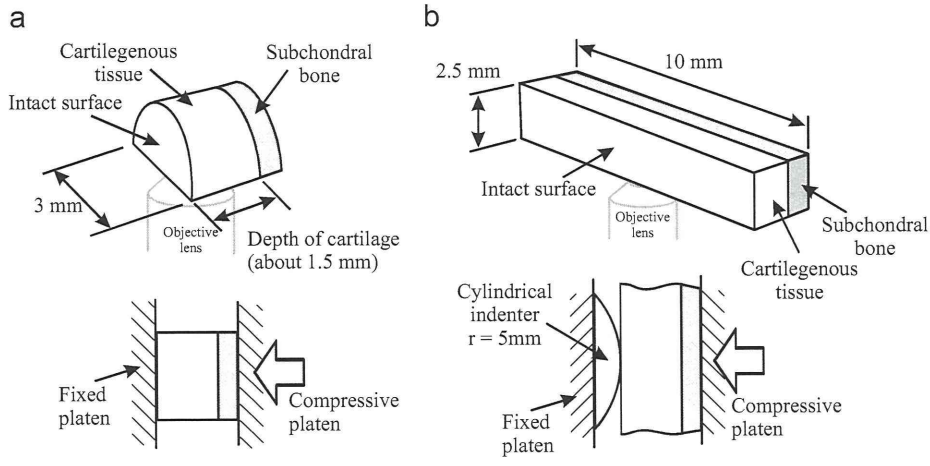

Fig. 2. (a) For the measurement of depth-dependent strain distribution, a 3 mm cylindrical core with subchondral bone was harvested by a biopsy punch and then split into the half perpendicular to the articular surface (Platen compression test). (b) For the indentation by the cylindrical indenter, a bar shaped osteochondral explant with the dimension of about 2.5 mm width and 10 mm length was dissected with preserving the intact surface.

specimen was compressed to the prescribed compressive distance at a constant velocity. Thereafter, the position of the compressive platen or the indenter was kept constant by the feedback position control for a stress relaxation period. During the test, the compressive load or the reaction force was monitored and fluorescence images were acquired as necessary.

2.2. Derivation of depth-dependent Young's modulus from experimental compressive test

The depth-dependent variation of Young's modulus of the solid phase was estimated by the platen compression of half-cylindrical specimen, shown in Fig. 2(a). Content of this section has been partly reported by our previous paper [44]. The specimen was put on the glass plate with facing the cut section of the punched cylindrical explant split half. In this experiment, the total compression of 10% of the depth of cartilaginous tissue and the compressive velocity of 1000 μm/s were employed as primary compressive motion, and then the platen was kept during stress relaxation for 30 min to ensure an equilibrium condition where the interstitial fluid nearly cease flowing. Fluorescent images before compression and at equilibrium condition were obtained by CLSM to estimate the local strain, which represents the variation of apparent compressive Young's modulus of solid phase along depth direction in the correlation of two images. Fig. 3 shows typical fluorescent images before compression and at equilibrium condition. The same cells were carefully identified in both images. In this situation, the local compressive strain ε is easily calculated from the change of the distance between corresponding pair of cells in fluorescent images using Eq. (1), where a and b are the distance of the cell-to-cell before compression and at equilibrium, respectively:

$$\varepsilon = \frac{a-b}{a} \tag{1}$$

The local strain $\varepsilon(x)$ was obtained as the function of depth position x ($0<x<1$; the position 0 means surface). Since the interstitial fluid pressure subsides to zero in equilibrium condition, it is considered that only solid phase carries compressive load in biphasic model. Under an assumption of disregarding the lateral deformation, total stress $\sigma_0=E_0\varepsilon_0$ as a property of entire specimen is equal to local stress σ in any depth position, where E_0 and ε_0 are total apparent Young's modulus of solid phase and total strain, respectively. The relationship between total stress and local stress in equilibrium state is given by $E_0\varepsilon_0=E(x)\varepsilon(x)$, where $E(x)$ is the depth-dependent Young's modulus. Thus $E(x)$ is given by

$$E(x) = \frac{\varepsilon_0}{\varepsilon(x)} E_0 \tag{2}$$

E_0 and ε_0 can be acquired from a total reaction of the tissue by the compressive testing apparatus and $\varepsilon(x)$ by the microscopic images written before. Note that the small Poisson's ratio of the solid phase in some literatures have been indeed applied or estimated as the value nearly 0 (Jurvelin et al. as 0.158 ± 0.148, Wilson et al. as 0.15, Warner et al. as 0.08, Graindorge et al. as 0, and Pawaskar et al. as 0.08) [17,32,35,39,42].

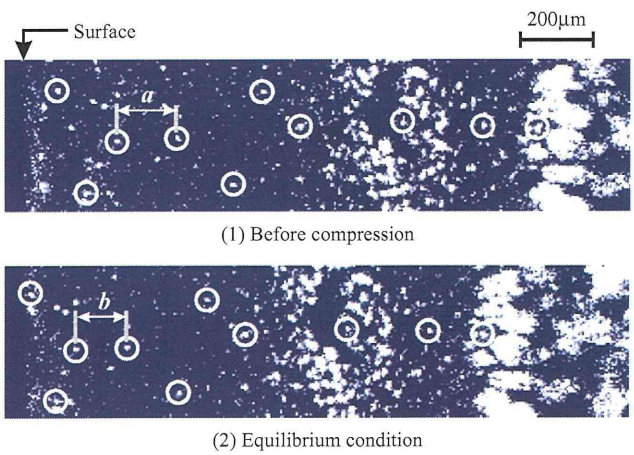

Fig. 3. Typical fluorescent images before compression and at equilibrium condition. The same cells were carefully identified in both images. Since these images were scanned with smallest pinhole of CLSM for an example, the number of cells seems to be small.

2.3. Experimental method for cylindrical indentation

The cylindrical indentation test was conducted to gain time-dependent reaction force for the estimation of constitutive material properties, whose were applied to the following FEM analysis. In this experiment, cylindrical indenter of 5 mm radius was pressed to the bar specimen shaped with about 2.5 mm width and 10 mm length shown in Fig. 2(b). The bar specimen was put on the glass plate of the compressive tester, in which intact surface of the cartilaginous tissue faced to the indenter. We could observe an image of the cutting section through microscope. The image was utilized to measure the depth of the cartilaginous tissue from the osteochondral specimen. In this study, the opposite of the sectional surface facing to the glass plate for microscopic observation was not constrained and the tissue was soaked in PBS during the experiment. Total compressive displacement of the indenter was 10% of the tissue depth at the cylindrical apex of the indenter. Compressive times were chosen as 2, 5, and 10 s to acquire the differences of the time-dependent reaction force including the peak force. Therefore, the compressive speeds were 5%, 2%, 1% per second, respectively. One specimen was sequentially used in the 3 different compressive speeds. After each compression trial, the specimen was soaked in PBS for 30 min to recover its water content and intact shape. Repeatability was checked prior to the experiment; however a disturbance on stable contact seemed equal to the variance of the repeatability. There are some differences in the cylindrical indentation from the platen compression configuration. One of the differences of cylindrical indentation is that the effect of surface seepage of water content should be incorporated into the reaction response.

2.4. Estimation of material properties

Material properties were specified by curve fitting comparing FEM calculation with experimental time-dependent reaction force of the cylindrical indentation. A commercial package ABAQUS (6.8-4), which was past appropriately evaluated for the biphasic analyses [45], was used in this study. Two-dimensional model was accepted to easily introduce consequent sliding motion of the cylindrical indenter shown in Section 2.5. Model geometry for estimating material properties was almost the same to the experimental configuration of the cylindrical indentation written in Section 2.3, shown in Fig. 4. The dimension of the model was 1.5 mm thickness and 10 mm length as a typical shape of the experimental specimens. The metallic cylindrical indenter (stainless steel) was of 5 mm radius represented by geometrical rigid body. The biphasic tissue was modeled by CPE4RP (four-node bilinear displacement and pore pressure, reduced integration with hourglass control) elements and the mesh size was chosen as 0.1 mm^2. The bottom of the model was fixed and impermeable, where no flow was allowed through the bottom surface. The other surfaces were not fixed and basically permeable except for the

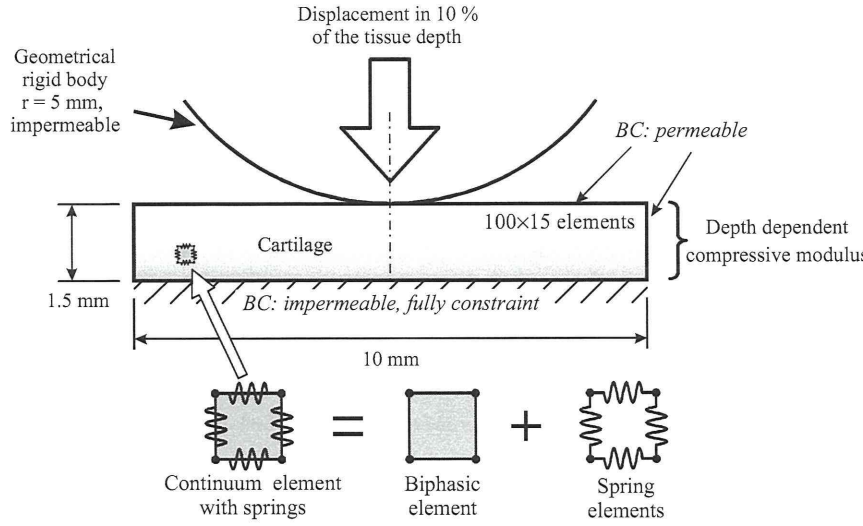

Fig. 4. The dimension of the model was 1.5 mm thickness and 10 mm length as a typical shape of the experimental specimen. The metallic cylindrical indenter was of 5 mm radius by geometrical rigid body. Horizontal and vertical fibrils were represented by a spring element SPRINGA.

contact region. The friction coefficient μ_{eq} [21] between the geometrical rigid indenter and the solid phase was set to zero. The compressive displacement was applied at the center of indenter with 10% of depth of the tissue model at the speed of the same 5%, 2%, 1% per second as that in experiment. It is important factor which constitutive properties are incorporated into representative material model for the calculation. In this study, we modeled the following constitutive compositions for the model. Firstly, the management of the surface seepage for exuding water content was implemented by user subroutine of ABAQUS using FLOW function (user subroutine to define nonuniform seepage coefficient and associated sink pore pressure for consolidation analysis). In the area covered by the cylindrical indenter the seepage coefficient of surface was set to zero to prevent flowing, whereas in the other area the seepage coefficient was set to one as a sufficient large value [46]. It was reported that the inhomogeneous cartilage property through depth direction promoted the effect of the interstitial fluid support [47]. Depth-dependent apparent Young's modulus of solid phase was introduced into our model, in which each layer in the FE model had each depth-specific modulus calculated by Eq. (2). It was expected that the effect of the surface amorphous layer [39] was partly incorporated in the depth-dependent Young's modulus in terms of a mechanical property, since Young's modulus of the top surface layer was lowest through depth direction in our observation shown later. Hydraulic permeability is well dependent as a function of strain [17]. For instance, Li incorporated the strain dependence of the permeability k into their FE model [24] by

$$k = k_0 \exp\left(M \frac{e-e_0}{1+e_0}\right) \tag{3}$$

where e_0 is an initial void ratio, e is the current void ratio, k_0 is the initial permeability at $e=e_0$, and M is a constant representing an effectiveness on the compaction. The initial void ratio e_0 as a constant value was set to 4, which represents that the proportion of the water content is 80%. Strain of solid phase is written by is $\varepsilon=(e-e_0)/(1+\varepsilon_0)$. Collagen fibril network, which was assumed to resist only tensile strain in this study, generates the sharp peak stress immediately after compression [24]. In recent computational analysis using spherical indenter, it was reported that deep vertical collagen fibril plays an important role on the reactional stiffness of the tissue especially in the transient period of a physiological condition [36]. In our model, as shown in Fig. 4, horizontal and vertical fibrils were represented by spring element SPRINGA (axial spring between two nodes, whose line of action is the line joining the two nodes) of the software, in which the spring elements were configured to generate reaction force only in the tensile direction. In this study, the stiffness K of the spring elements was simplified to the uniform value over the tissue and both in horizontal and vertical direction.

In summation, the variables for the curve fitting on FEM calculation were total apparent Young's modulus E_0, initial permeability k_0, compaction effect on permeability M, and collagen stiffness K. In other words, we tried to reduce the representation of the time-dependent reaction force of the cartilaginous tissue into these 4 variables within our compressive configuration, which aimed at a physiological condition in terms of compressive speed and amount. Depth-dependent local strain $E(x)$ was separately acquired as a typical value by the platen compression test written in Section 2.2. The curve fitting was executed by repetition of trial calculations and by visual confirmation with superposing the calculations on the experimental results. The threshold for automatic time integration in the estimation of material properties was specified of 10 kPa for UTOL, which regulates time integration period not to exceed the change of pore pressure by UTOL value within one increment. The NLGEOM parameter was turned on to take account of geometrical nonlinearity. Note again that the experimental results for estimating material properties were acquired from definite displacement compression by a positional control of the cylindrical indenter.

2.5. Finite element analysis for sliding cylindrical indenter

The constitutive material properties estimated and modeled in Section 2.4 were consequently applied to the analysis of sliding cylindrical indenter over cartilage surface. The dimension of the tissue model used in this section was 1.5 mm thickness and 25 mm length, shown in Fig. 5. The metallic cylindrical indenter that was slid over cartilage surface was of 5 mm radius. The biphasic tissue was modeled by CPE4RP and the mesh size was chosen as 0.1 mm square. Hence the total number of the elements was 3750 (250×15). The bottom of the model was fixed and impermeable. The other surface was not fixed and basically permeable except for contact region, in which the seepage coefficient within contact

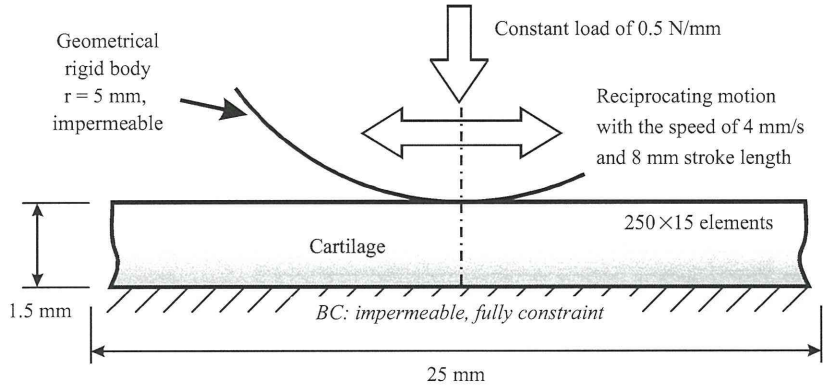

Fig. 5. The load of 0.5 N/mm was applied at the center of the cylindrical indenter and then the load was held constant. The reciprocating motion was introduced for the loaded indenter with the speed of 4 mm/s over a stroke length of 8 mm.

region was set to zero as written previously. One of the differences of compressive condition from Section 2.4 was that the indentation was performed by force, not position. The load of 0.5 N/mm was applied at the center of the cylindrical indenter with a ramp time of 1 s and then the load was held constant for further 92 s. Initial horizontal position of the indenter was at the center of the tissue surface. In the condition of sliding cylindrical indenter, the reciprocating motion was introduced for the loaded indenter with the speed of 4 mm/s over the stroke length of 8 mm during 92 s, which results in 23 cycles of reciprocation. In order to evaluate the sliding effect on the interstitial fluid pressurization, the static loading of the same 0.5 N/mm over entire period of simulation was also examined without any sliding motion in the simple creep-deformation simulation by the cylindrical indenter. The threshold for automatic time integration during the sliding period was specified of 1000 kPa for UTOL due to the limitation of calculation time, however maximum length of time integration was limited to 0.05 s. The other parameters were equal to the model in Section 2.4.

3. Results

3.1. Measurement of local strain

It is known that equilibrium local strain of cartilage tissue in compressive test varies from articular surface to deep zone, in which the surface zone is largely deformed in equilibrium condition [13,15,16]. In this study, a single image set on the relation between before compression and at equilibrium condition was examined to obtain local strain distribution through depth direction. Fig. 6(a) shows the local compressive strain plotted in normalized depth position, in which the position 0 means the surface. The average strain of the solid phase ε_0 was 9.90% in this experiment. Using Eq. (1), the local strain $\varepsilon(x)$ was acquired as the function of relative position x by

$$\varepsilon(x) = 0.462e^{-6.53x} + 0.0284 \quad (4)$$

It was observed that the tissue near the top surface was largely compressed by more than 40% strain. In this study, only $\varepsilon(x)$ and ε_0 were utilized in following FEM study to determine the variation of Young's modulus $E(x)$ through depth direction using Eq. (2).

3.2. Estimation of material property using FEM

In considering that the cylindrical indenter was used for the estimation of material properties, it would be appropriate that the

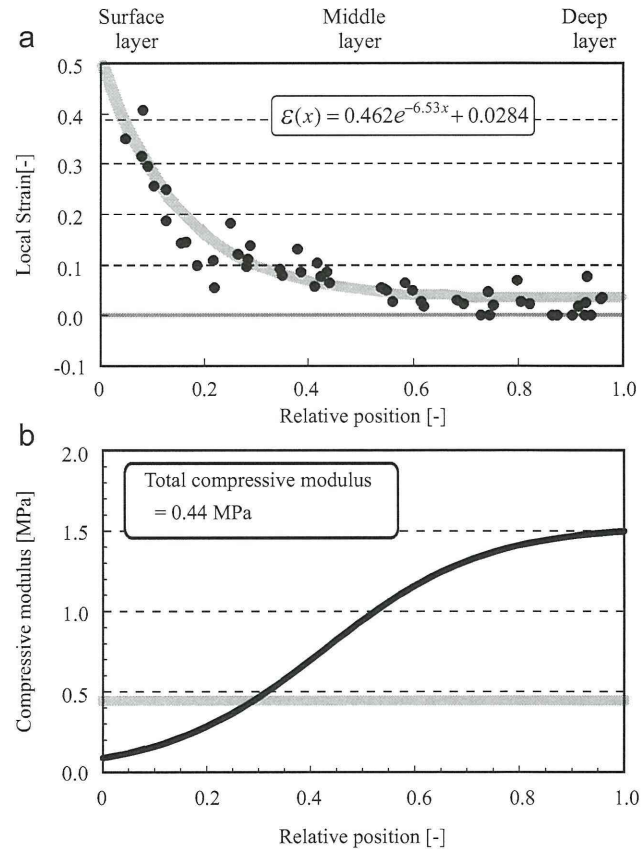

Fig. 6. (a) The local strain distribution through depth direction. The average strain of the solid phase was estimated by 9.90% in this experiment. (b) Compressive modulus distribution, when the bulk modulus is 0.44 MPa.

reaction force (not stress) was suitable for evaluating the curve fitting. Fig. 7 shows the experimental results of the cylindrical indentation (N=9), variance of experimental data and the results of curve fitting by the FEM calculation. The depth of the cartilaginous tissue of subchondral specimens, the width and the length were 1.53 ± 0.14, 2.48 ± 0.19, and 8.46 ± 1.95 mm (average $\pm$ variance), respectively. Note that the resultant curve fittings in different compressive speed shown in Fig. 7(a)–(c) were derived from the single parameter set of the material properties estimated in this study. The curve fitting was generally performed by following procedure, which may include an insightful affair on

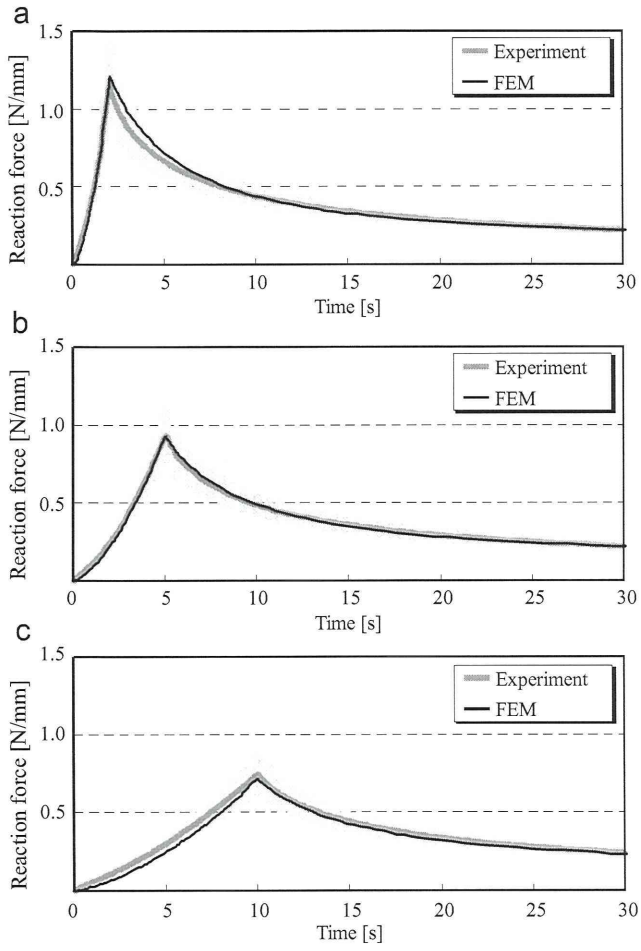

Fig. 7. The experimental results of the cylindrical indentation ($N=9$), variance of experimental data and the results of curve fitting of FEM calculation. Total compressive displacement of the indenter was 10% of the tissue depth at the cylindrical apex of the indenter. (a) 2 s, (b) 5 s and (c) 10 s compression.

how each parameter representing constitutive material property works functionally over the time-dependent reaction force.

As the time approaches to equilibrium period, the total compressive Young's modulus predominantly governs the total reaction force, because interstitial fluid pressure subsides. The total apparent Young's modulus of the solid phase E_0 was approximately estimated by the experimental reaction force at 180 s (not shown in this report). Then, the combination of $\varepsilon(x)$ and ε_0 with E_0 provides the distribution of apparent Young's modulus $E(x)$ for the curve fitting, by Eq. (2). Since the peak reaction force at the end of the compressive motion is clearly sensitive to the spring stiffness K, the spring stiffness was roughly identified here. Consequently, the rapid decrease of the reaction force immediately after compression for about 4 s well represents a relatively larger value of the initial permeability k_0. Without the compaction effect from the parameter M in Eq. (3), stress relaxation seemed to be faster than that of the experimental result. The modulation of the parameter M leads to the adjustment of stress relaxation in latter period. The repetition of these procedures would recurrently result in an acceptable curve fitting between the experimental result and the FEM calculation. Although small corrections of the parameters were required for the good fitting over different compressive speed, the curve fitting for 5 s compression shown in Fig. 7(b) basically found a reasonable value over the other compressive speed. While the objective data for the curve fitting on estimating the representative material properties was an average of time-dependent reaction force from 9 specimens, the data by a single specimen also showed fine fitting to FEM calculation over the different compressive speeds. The resultant parameters are shown in Table 1. Although the permeability of initial condition k_0 of 29.43×10^{-15} m^4/N s might be relatively larger value than a typical value of the permeability in other FEM research, large value for the initial permeability have been reported in some past research, in which the permeability was estimated by fitting FEM calculation to experimental result [17]. From our result with the parameter M of 38, the value $K=2.0\times10^{-15}$ m^4/N s is obtained in the compressive strain of 7% by Eq. (3). If the total apparent Young's modulus of the solid phase E_0 has the resultant value of 0.44 MPa, the distribution of apparent Young's modulus along the depth direction is plotted as shown in Fig. 6(b).

3.3. FEM analysis on the effect of migrating contact area and the constitutive parameters

Fig. 8 shows the result of FEM simulation on the effect of migrating contact area and the constitutive parameters. Index character A–E represents which the constitutive components were included in the FE model, shown in Fig. 8(b); e.g. the character E indicates that the distribution of compressive Young's modulus, the compaction effect on permeability and the reinforcement of spring elements were included in the model. If the distribution of apparent Young's modulus along depth direction was not included in the model, the apparent Young's modulus of 0.44 MPa as a bulk property was homogeneously applied to all the elements. If the compaction effect on permeability was not included, permeability in the model always remained in the initial value k_0. The vertical axis of the bar graphs in Fig. 8 represents the supporting force N/mm by the tissue. Total load support in each condition was summed up to 0.5 N/mm, because normal load of the indenter was held constant by 0.5 N/mm after the first compressive loading. Percentage numbers attached just above the bar graphs show the proportion of fluid load support to the total load.

Fig. 8(a) shows the proportion of load support immediately after compression of 1 s ramp loading. The distribution of apparent Young's modulus of the solid phase promoted the ratio of the fluid support. The reinforcement by spring elements was also effective to enlarge the ratio of the fluid support in comparing the conditions D with B. Fig. 8(c) shows the load support at 92 s after the end of ramp loading in the case that the indenter did not move from initial horizontal position. The compaction effect on permeability sustained the fluid support in comparing the conditions C and E with the others. In the condition without the compaction effect, permeability was constant in the initial permeability k_0. The value k_0 was thought to be a peculiar one in which the tissue was fully swelled on the surface of the bulk

Table 1
Material and kinematic properties estimated and used in the model of a cylindrical indenter sliding over cartilage.

Parameter	Value
Young's modulus (E_0)	0.44 MPa
Poisson's ratio	0.125
Initial permeability (k)	29.43×10^{-15} m^4/N s
Compaction effect on permeability (M)	38
Void ratio	4.0 (80% interstitial fluid)
Spring stiffness (K)	3.5 MPa
Sliding velocity	4 mm/s
Sliding stroke	$\pm$4 mm about the center
Seepage coefficient	1 mm^3/N s—flow 0 mm^3/N s—no flow,
Normal load on indenter	0.5 N/mm

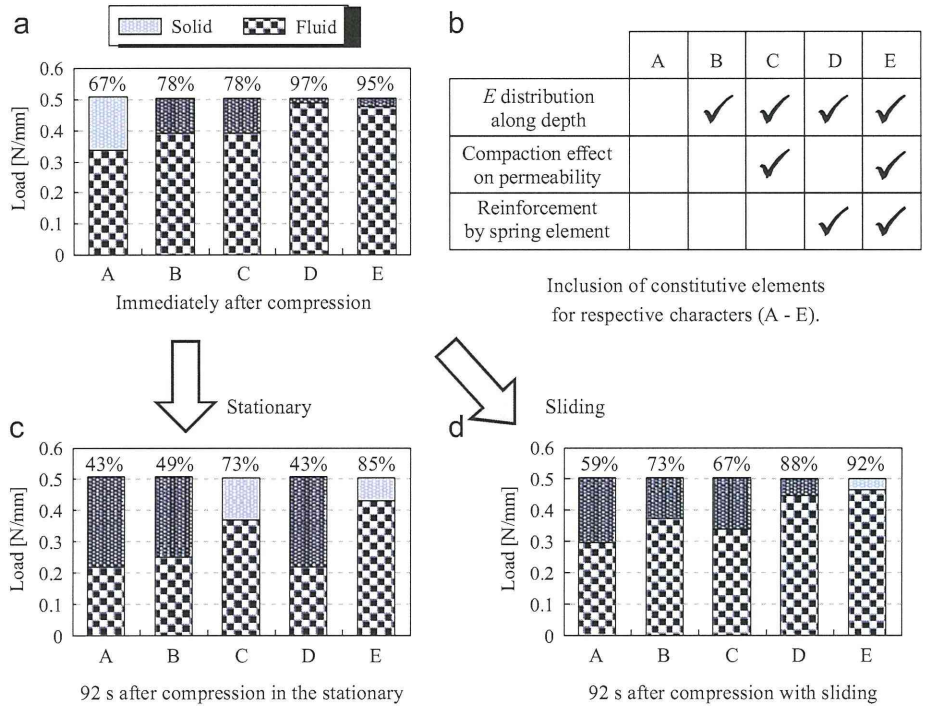

Fig. 8. (a) The result of FEM simulation on the effect of migrating contact area and the constitutive parameters. (b) Index characters A–E represents the constitutive components included in the FE model. The bar graph (a) shows the proportion of load support at immediately after compression. The graphs (c) and (d) show that of stationary indenter and moving indenter at 92 s, respectively.

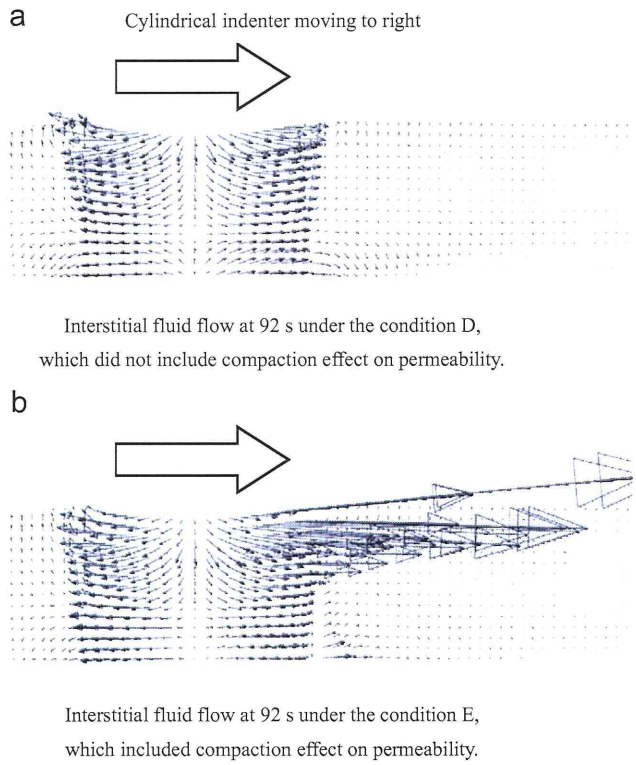

Fig. 9. Interstitial fluid flow at 92 s where the indenter was moving right. The compaction effect on permeability seemed to change the fluid flow.

tissue. Relative lower ratio of the fluid support in the condition D may be caused by this peculiar value k_0. Fig. 8(d) shows the load support with the sliding motion of the cylindrical indenter.

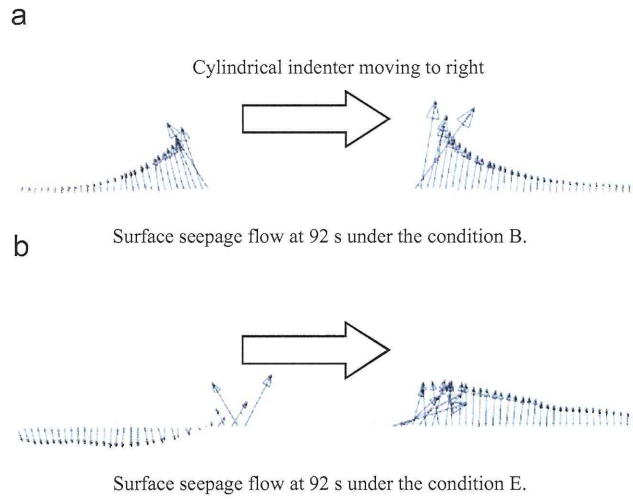

Fig. 10. The surface seepage of the flow. In this figure, the scale of the arrow representing fluid flow is 20 times larger than that in Fig. 9. The model including the spring reinforcement, which represents the collagen network, showed the drawing of the fluid behind the indenter. In this figure, the elements just under the contact area were removed to easy visibility for the surface seepage.

The time period of 92 s means that the indenter locates at the horizontal center of the tissue surface after 23 cycles of reciprocating motion. In sliding condition, the rubbing surface experienced a re-swelling period, since the contact area migrated over the tissue surface. As a whole, the fluid support was increased in comparing Fig. 8(c) except for the condition C. While the condition D drastically improved the ratio of the fluid load support, the condition C slightly decreased the fluid load support.

In observing interstitial fluid flow, the model including the compaction effect on permeability showed a particular flow

distribution, in which the interstitial fluid near the surface flowed forward in the moving direction of the cylindrical indenter. A typical result is shown in Fig. 9. The scale of the arrow representing fluid flow is the same in Fig. 9(a) and (b). This particular flow was probably due to the quick decrease of the permeability from the compaction effect written by Eq. (3), because the forward region was not so compressed than the region just under the apex of the cylindrical indenter. In observing the seepage flow on the tissue surface, the model including the reinforcement by spring elements showed an interesting result. The model including the spring reinforcement exuded the interstitial fluid in the forward surface of the indenter, whereas the fluid flow in the backward region was drawn in the tissue near the indenter shown in Fig. 10. This phenomenon was obscure in the model without the reinforcement by spring elements, which hopefully represents the tensile strengthening of the cartilaginous tissue by the collagen network.

4. Discussion

In the measurement of local strain at equilibrium state, large compressive strain was observed near the tissue surface. Apparent compressive Young's modulus was estimated under unconfined compression of semi-cylindrical specimen. The research concerning the inhomogeneity of the compressive modulus had been studied by several researchers. The method for estimating local strain by the correlation of microscopic images was utilized to estimate depth-dependent local strain without cutting the tissue into the stack of thin slices through depth direction. Using image correlation method, variation of the equilibrium local strain of full-thickness articular cartilage with subchondral bone was estimated in the past by a confined compression setup by Schinagl. In terms of aggregate modulus, the compressive modulus of first 125 μm layer from intact surface and the 250 μm thick layer adjacent to the subchondral bone were reported by 0.21 times and 5.6 times of the total bulk compressive modulus, respectively [13]. The local strain data from full-thickness tissue was consequently incorporated in a FE model to analyze stress relaxation behavior on the effect of depth-dependent compressive modulus [28]. Although an unconfined compression of semi-cylindrical osteochondral specimen was conducted in this study, the apparent compressive Young's modulus at surface and at bottom of the full-thickness articular cartilage were estimated to be 0.20 and 3.4 times of the total bulk property with a small extrapolation shown in Fig. 6(b). In a similar unconfined compression of semi-cylindrical geometry being removed subchondral bone, the compressive Young's modulus in the deep layer was reported to be about 2 MPa and had up to 10 times larger value than that in the surface layer [15]. In this study, a single data from one correlative image set was managed to find the local strain distribution for mainly re-confirming previous reports. Although absolute value was not completely congruent with the result of the other reports, the relative value of the compressive modulus in the surface layer to the bulk modulus was not so different from that shown in other report. Actually, the total apparent Young's modulus E_0, which regulated the absolute value of $E(x)$ shown in Eq. (2), was estimated from our experimental data by curve fitting using FEM simulation shown in Fig. 7, whereas the local strain distribution $\varepsilon(x)$ was utilized to transform the value E_0 into Young's modulus distribution $E(x)$. Since the purpose of this study is to examine how the constitutive material properties express the function of the cartilaginous tissue as a load-bearing material, authors thought that the local strain distribution acquired in this study would be acceptable in terms of the analysis concerning the integration of each constitutive mechanical property.

The identification of material properties utilizing the curve fitting was achieved with visually good conformation to the experimental data by the insightful procedure written in Section 3.2. From our experiences, we never succeeded in fitting FEM result to the time-dependent reaction force of the experimental indentation test without the effect of the compaction on permeability. In this study, four constitutive parameters, total apparent Young's modulus E_0, initial permeability k_0, compaction effect of permeability M and collagen stiffness K, were included for reproducing the mechanical behavior of articular cartilage in terms of the time-dependent reaction force. In this experiment, the influence of surface seepage was included by the geometrical condition of the cylindrical indenter. Although we could not insist that these parameters represented almost all mechanical behavior of the cartilaginous tissue, it was notable that the representation of the tissue in this study well conformed to the three different time-dependent reaction force in relatively physiological compressive speed. There would be generally 3 types of reason on dispersing experimental data. Firstly, there was a dispersion derived from an individual difference of each tissue. In looking into a single trial, the peak stress at the end of the ramp compression seemed to be very sensitive to compressive speed and displacement. Initial short load of 0.05 N just before the compression was applied to make sure a stable contact. Moreover, each specimen was exposed to three different compressive speeds following swelling interruption, where repeatability of the experiment was consistently required. Precise control of compressive speed and displacement was appropriately performed in the electro-mechanical tester with feedback control developed in our laboratory. While we experienced fine fitting of the reaction force between the experimental result and the FEM simulation, experimental data by single specimen basically showed the same level of fine fitting to FEM calculation over the different compressive speeds.

The initial permeability k_0 was estimated to be a relatively larger value than that in another report that utilized curve fitting of FEM simulation [24]. On the other hand, Jurvelin reported the permeability of a large value in small compressive strain and a drastic change of the permeability as the function of strain [17]. One of the reasons why the large initial permeability was estimated in this study might belong to the geometry of the cylindrical indentation, in which the surface seepage of the interstitial fluid was allowed just around the indenter. In other words, the surface for the exudation was simply large near the indenter or near the path of fluid flow. A degree of swelling was also the factor of variance on the initial permeability, which might include an osmotic phenomenon. In this study, the specimen was soaked in PBS for 30 min after compression test to recover shape and swelling level of the tissue in considering small size of the specimen. The inclusion of compaction effect on permeability successfully improved the conformity of the curve fitting. We applied 10% strain at the apex of the cylindrical indenter in experimental compression test. Although the compaction effect in larger strain field was not assured in this study, the effect above 10% strain was extrapolated by Eq. (3).

In all FE model employed in the curve fitting and consequent sliding simulation, Poisson's ratio of 0.125 for the solid phase was accepted as a typical value. It was thought that Poisson's ratio of the cartilaginous tissue varies through depth direction with anisotropic property. Since subchondral bone was preserved in our experimental specimens, lateral deformation of the bottom layer was constrained by the presence of subchondral bone. Cartilage-on-bone structure affects its micro-anatomical response on internal strain distribution [48]. The constraint of the bottom zone in compression test should apparently stiffen the tissue, while Poisson's ratio of the surface zone was reported as a small value, e.g. about 0.05 [15]. Our experimental observation for

estimating local strain distribution was examined in this complex phenomenon. Therefore, Young's modulus distribution in our report may apparently be a medial value between the results of confined and unconfined compression. While many different values were employed for Poisson's ratio with respective insights, we simply borrowed the value of 0.125 as a reasonable value, which was past used in some FE model [49]. In any case, in considering dynamic transient condition studied in this paper, the spring element representing the collagen network predominantly resists the lateral deformation caused by interstitial fluid pressure in the platen compression test.

Solid phase of the tissue is subjected to the interstitial fluid pressure including the osmotic pressure in addition to the compressive forces as a load-bearing. The collagen network reinforces the solid phase and resists mainly tensile deformation. The cartilaginous tissue involves tension–compression nonlinearity [3–5]. The structural combination of swelling plenty water content and binding the collagen network under the low permeability produces the high pressure of the interstitial fluid, which offers considerable contact load supported by the fluid phase and reduces solid-to-solid frictional force. The mechanical function of the collagen network is a significant factor in considering biphasic lubrication. The collagen network in the tissue has depth-specific anisotropy and inhomogeneity. The FE model in this study included horizontal and vertical spring for representing the collagen network. In the platen compression test, it is thought that the vertical collagen expresses little of its functionality. However, the vertical collagen fibril specially functions in spherical or cylindrical indentation in transient period. The presence of the vertical fibril increased the transient stiffness of the cartilage and the interstitial fluid pressure [40]. Authors confirmed the role of the vertical fibril (not shown in the present paper), in which the vertical fibril resisted vertical bulge that would have been caused by the interstitial fluid pressure around the indenter. Then, the restraint of vertical bulge by vertical fibril enhanced the interstitial fluid pressure. Although we realizes that the morphology of collagen network should have some function as a load-bearing, authors decided to apply homogeneous and isotropic arrangement of the spring elements representing the collagen network in the model, because of the complexity. This point was a limitation of this study. However, the inclusion of the vertical fibril in the model should play a significant role especially in the condition of the sliding cylindrical indenter.

The FEM survey on how much the constitutive properties of the model sustained the proportion of fluid support showed a comprehensible result shown in Fig. 8. Migrating contact area delivers a time period to re-swell the tissue. Pawaskar reported that the proportion of load support by the pore pressure was maintained in the configuration with the metallic cylindrical indenter sliding on cartilage surface in FEM simulation [42]. By experimental friction tests, Caligaris reported that migrating contact area significantly promoted sustainability of the interstitial fluid pressurization mechanism and consequent low friction coefficient [41]. Within the condition A shown in Fig. 8, the sliding condition showed larger proportion of the fluid load support than stationary one. In this study, FEM calculation of the condition A was almost equal to that by Pawaskar's report except for large permeability value, which was set to the initial permeability k_0 having 7.5 times larger value than Pawasker's one. Although the proportion of fluid load support was lower than that of the previous paper, which reported 81% of total contact load, sliding condition exceedingly prevented declination of the proportion of fluid load support. The inclusion of Young's modulus distribution also promoted the proportion of fluid load support in comparing the conditions A with B in Fig. 8. This phenomenon was past suggested in the previous study [46], which included depth-dependent properties on every constitutive parameter. Very low Young's modulus in the top layer may be partly included the effect on biphasic surface amorphous layer [39], which was discussed with an effect on repeated dynamic loading.

Inclusion of the compaction effect on permeability showed an interesting result. In Fig. 8(a), the compaction effect to the fluid support was not seen in comparing the conditions C with B. In Fig. 8(d), the compaction effect did not promote the fluid load support in the sliding condition. However, the compaction effect to the fluid load support clearly arose in the stationary condition shown in Fig. 8(c). Of course, it was obvious that the transition to lower permeability by the compaction effect suppressed the fluid flow and caused higher proportion of the fluid load support, because the condition B remained to the initial permeability value k_0. We had better consider that the compaction effect on permeability did not well promote the interstitial fluid load support especially in the sliding condition. There arises a question why the compaction effect on permeability exists in the properties of the articular cartilage. The lower compressive modulus in surface layer normally promotes the proportion of fluid load support, whereas the constitution of the lower compressive modulus of the solid phase may not be able to maintain lower permeability in the actual tissue. Therefore, the compaction effect on permeability would be a substitutional property to increase the fluid support in the condition of the stationary contact. However, it should be additionally noted that in severe sliding condition with short stroke without sufficient re-hydration, the deformation will become larger and thus the compaction effect on permeability may be effective.

The reinforcement of solid phase by the spring elements representing the collagen network significantly promoted the interstitial fluid load support in sliding condition. The representation of collagen network was discussed in the past, in which sharp reaction force was observed at immediately after compression by the inclusion of tensile reinforcement [24,40]. It is clearly thought that the sliding condition is one of the dynamic conditions. Finally, the condition E shown in Fig. 8 resulted in most superior proportion of the fluid load support in both stationary and sliding condition.

It may be too premature to discuss the interstitial fluid flow, because some of characteristic constitution in the cartilaginous tissue was not completely represented in our model, especially on the depth-dependent inhomogeneity and anisotropy of the collagen network. However, a peculiar fluid flow, typically shown in Fig. 9, was observed in the conditions C and E, which included the compaction effect on permeability. Although it was difficult to interpret the peculiar internal fluid flow at present state, the inclusion of the compaction effect altered the dynamics of fluid flow in surface to middle zone. From the observation of micro-anatomical response of cartilage-bone constitution, a chevron discontinuity under rectangular indentation was reported with an affair of the potential for delamination to occur in the upper region of cartilage [47]. The mechanics in this region should be still a future problem. Inclusion of the spring element representing the collagen network, which was specified by the conditions D and E in Fig. 8, clearly showed the drawing of fluid into cartilage tissue behind the sliding motion near the cylindrical indenter, typically shown in Fig. 10(b). In the cartilage surface far from the indenter, a small drawing of the fluid was observed over a wide range in any sliding condition. The inclusion of the spring reinforcement promoted the drawing of the fluid in near the high fluid pressure just under the indenter.

There are some limitations in this study. Today, more detailed FE models [24–34] were proposed, e.g. inhomogeneity and anisotropy of the collagen network and the permeability, osmotic pressure and its electrical current flow, viscoelasticity of the matrix, nonlinearity of the collagen in tensile direction and so on. The physiological contact geometry and load [35] was not examined. We believe that more detailed model should find another new functionality on the

integration of constitutive material property, while the experimental observation has to be continued to acquire appropriate insights and actual phenomena. In this study, the behavior of tissue matrix under the sliding condition was not observed experimentally. To evaluate the FEM simulation, a new experimental tester to observe internal strain field under sliding indenter will be developed in near future as a series of this study.

The methodology of this study may have an obscure part. The curve fitting was executed by the repetition of visual confirmation shown in Fig. 7. Although authors experienced acceptable orthogonality of the parameters for representing material properties as described in Section 3.2, inclusion of another extra parameter may result in uncertain identification of the material parameters as long as the method in curve fitting will not be advanced. More distinct method should be incorporated in the curve fitting procedure, e.g. the least-square method. It was thought that the time of 92 s for sliding or stationary load was still transient period. In ABAQUS (version 6.8-4), the time integration length is partly controlled by the parameter UTOL. In this study, UTOL of 1000 kPa was set in sliding period in our calculation, while Pawaskar specified UTOL of 600 kPa in their sliding simulation [42]. However, time integration length was controlled around 0.01 s by the version of ABAQUS used in this study, while maximum time integration length was restricted in about 0.05 s. Moreover, the two-dimensional model was used instead of three-dimensional model in order to reduce computational time. The spring elements representing collagen network were spread in vertical and horizontal direction in the model. In this situation, the spring elements did not work in pure parallelogram deformation. Therefore, arguments in this report may partly be closed in a qualitative one in present state. The specimen used in this study was harvested from porcine knee joint of 6–8 months old. Since degree of mature affects biomechanical properties [50,51], we should consider that the experimental data in this study was the data from relatively immature tissue.

5. Conclusion

In this study, the effect of constitutive properties of the cartilaginous tissue as a biphasic material was investigated mainly on how the existence of constitutive material properties affects the proportion of the fluid support in contact area. Time-dependent reaction force was acquired experimentally by cylindrical indentation, which had almost equal geometry to the FEM simulation. The FE model simulation identified material properties by the curve fitting method. In consequent sliding simulation, the reinforcement by spring elements and depth-dependent elastic properties were significantly effective in interstitial fluid pressurization. The compaction effect on the permeability did not show clear improvement on sustainability of the interstitial fluid support in sliding configuration, whereas the compaction effect arose in stationary indentation configuration.

Acknowledgment

Financial support was partly given by the Grant-in-Aid for Scientific Research (A) of Japan Society for the Promotion of Science (21246029) and the Bilateral Joint Research Project with UK supported by Japan Society for the Promotion of Science.

References

[1] Ateshian GA. The role of interstitial fluid pressurization in articular cartilage lubrication. J Biomech 2009;42:1163–76.
[2] Katta J, Jin Z, Ingham E, Fisher J. Biotribology of articular cartilage—a review of the recent advances. Med Eng Phys 2008;30:1349–63.
[3] Huang CY, Soltz MA, Kopacz M, Mow VC, Ateshian GA. Experimental verification of the roles of intrinsic matrix viscoelasticity and tension–compression nonlinearity in the biphasic response of cartilage. J Biomech Eng—Trans ASME 2003;125:84–93.
[4] Chahine NO, Wang CCB, Hung CT, Ateshian GA. Anisotropic strain-dependent material properties of bovine articular cartilage in the transitional range from tension to compression. J Biomech 2004;37:1251–61.
[5] Ateshian GA, Hung CT. The natural synovial joint: properties of cartilage. Proc Inst Mech Eng H: J Eng Med 2006;220:657–70.
[6] Klein J. Molecular mechanisms of synovial joint lubrication. Proc Inst Mech Eng J: J Eng Tribol 2006;220:691–710.
[7] Graindorge S, Ferrandez W, Ingham E, Jin Z, Twigg P, Fisher J. The role of the surface amorphous layer of articular cartilage in joint lubrication. Proc Inst Mech Eng H: J Eng Med 2006;220:597–607.
[8] Murakami T, Higaki H, Sawae Y, Ohtsuki N, Moriyama S, Nakanishi Y. Adaptive multimode lubrication in natural synovial joints and artificial joints. Proc Inst Mech Eng H: J Eng Med 1998;212:23–35.
[9] Murakami T, Nakashima K, Sawae Y, Sakai N, Yarimitsu S, Hosoda N. Roles of adsorbed film and gel layer in hydration lubrication for articular cartilage. Proc Inst Mech Eng H: J Eng Med 2009;223:287–95.
[10] Crockett R, Roos S, Rossbach P, Dora C, Born W, Troxler H. Imaging of the surface of human and bovine articular cartilage with ESEM and AFM. Tribol Lett 2005;19:311–7.
[11] Yarimitsu S, Nakashima K, Sawae Y, Murakami T. Influences of lubricant composition on forming boundary film composed of synovia constituents. Tribol Int 2009;42:1615–23.
[12] Guilak F, Ratcliffe A, Mow VC. Chondrocyte deformation and local tissue strain in articular cartilage: a confocal microscopy study. J Orthop Res 1995;13:410–21.
[13] Schinagl RM, Gurskis D, Chen AD, Sah R. Depth-dependent confined modulus of full-thickness bovine articular cartilage. J Orthop Res 1997;15:499–506.
[14] Chen AC, Bae WC, Schinagl RM, Sah RL. Depth- and strain-dependent mechanical and electromechanical properties of full-thickness bovine articular cartilage in confined compression. J Biomech 2001;34:1–12.
[15] Wang CCB, Deng JM, Ateshian GA, Hung CT. An automated approach for direct measurement of two dimensional strain distributions within articular cartilage under unconfined compression. J Biomech Eng—Trans ASME 2002;124:557–67.
[16] Erne OK, Reid JB, Ehmke LW, Sommers MB, Madey SM, Bottlang M. Depth-dependent strain of patellofemoral articular cartilage in unconfined compression. J Biomech 2005;38:667–72.
[17] Jurvelin JS, Bushmann MD, Hunziker EB. Mechanical anisotropy of the human knee articular cartilage in compression. Proc Inst Mech Eng H: J Eng Med 2003;217:215–9.
[18] Wang CCB, Chahine NO, Hung CT, Ateshian GA. Optical determination of anisotropic material properties of bovine articular catrilage in compression. J Biomech 2003;36:339–53.
[19] Mow VC, Kuei SC, Lai WM, Armstrong CG. Biphasic creep and stress relaxation of articular cartilage in compression: theory and experiments. J Biomech Eng—Trans ASME 1980;102:73–84.
[20] Park S, Krishnan R, Nicoll SB, Ateshian GA. Cartilage interstitial fluid load support in unconfined compression. J Biomech 2003;36:1785–96.
[21] Ateshian GA. A theoretical formulation for boundary friction in articular cartilage. J Biomech Eng—Trans ASME 1997;119:81–6.
[22] Ateshian GA, Wang H, Lai WM. The role of interstitial fluid pressurization and surface porosities on the boundary friction of articular cartilage. J Tribol—Trans ASME 1998;120:241–8.
[23] Krishnan R, Kopacz M, Ateshian GA. Experimental verification of the role of interstitial fluid pressurization in cartilage lubrication. J Orthop Res 2004; 22:565–70.
[24] Li LP, Soulhat J, Buschmann MD, Shirazi-Adl A. Nonlinear analysis of cartilage in unconfined ramp compression using a fibril reinforced poroelastic model. Clin Biomech 1999;14:673–82.
[25] Li LP, Soulhat J, Buschmann MD, Shirazi-Adl A. A fibril reinforced nonhomogeneous poroelastic model for articular cartilage: inhomogeneous response in unconfined compression. J Biomech 2000;33:1533–41.
[26] Soltz MA, Ateshian GA. A conewise linear elasticity mixture model for the analysis of tension–compression nonlinearity in articular cartilage. J Biomech Eng—Trans ASME 2000;122:576–86.
[27] Huang CY, Mow VC, Ateshian GA. The role of flow-independent viscoelasticity in the biphasic tensile and compressive responses of articular cartilage. J Biomech Eng—Trans ASME 2001;123:410–7.
[28] Wang CCB, Hung CT, Mow VC. An analysis of the effects of depth-dependent aggregate modulus on articular cartilage stress-relaxation behavior in compression. J Biomech 2001;34:75–84.
[29] Wilson W, van Donkelaar CC, van Rietbergen B, Ito K, Huiskes R. Stress in the local collagen network of articular cartilage: a poroviscoelastic fibril-reinforced finite element study. J Biomech 2004;37:357–66.
[30] Wilson W, van Donkelaar CC, van Rietbergen B, Huiskes R. A fibril-reinforced poroviscoelastic swelling model for articular cartilage. J Biomech 2005;38: 1195–204.
[31] Federico S, Grillo A, Rosa GL, Giaquinta G, Herzog W. A transversely isotropic, transversely homogeneous microstructual-statistical model of articular cartilage. J Biomech 2005;38:2008–18.

[32] Wilson W, van Donkelaar CC, Huyghe JM. A comparison between mechano-electrochemical and biphasic swelling theories for soft hydrated tissues. J Biomech Eng—Trans ASME 2005;127:158–65.
[33] Ateshian GA, Chahine NO, Basalo IM, Hung CT. The correspondence between biphasic and triphasic material properties in mixture models of articular cartilage. J Biomech 2004;37:391–400.
[34] Sun DD, Guo XE, Likhitpanichkul M, Lai WM, Mow VC. The influence of the fixed negative charges on mechanical and electrical behaviors of articular cartilage under unconfined compression. J Biomech Eng—ASME 2004; 126:7–16.
[35] Warner MD, Taylor WR, Clift SE. Finite element biphasic indentation of cartilage: a comparison of experimental indenter and physiological contact geometry. Proc Inst Mech Eng H: J Eng Med 2001;215:487–96.
[36] Shirazi R, Shirazi-Adl A, Hurtig M. Role of cartilage collagen fibrils networks in knee joint biomechanics under compression. J Biomech 2008;41:3340–8.
[37] Park S, Hung CT, Ateshian GA. Mechanical response of bovine articular cartilage under dynamic unconfined compression loading at physiological stress level. Osteoarthritis Cartilage 2004;12:65–73.
[38] Krishnan R, Mariner EN, Ateshian GA. Effect of dynamic loading on the frictional response of bovine articular cartilage. J Biomech 2005;38:1665–73.
[39] Graindorge S, Ferrandez W, Jin ZM, Ingham E, Fisher J. The natural synovial joint: a finite element investigation of biphasic surface amorphous layer lubrication under dynamic loading condition. Proc Inst Mech Eng J: J Eng Tribol 2006;220:671–81.
[40] Shirazi R, Shirazi-Adl A. Deep vertical collagen fibrils play a significant role in mechanics of articular cartilage. J Orthop Res 2008;26:608–15.
[41] Caligaris M, Ateshian GA. Effect of sustained internal fluid pressurization under migrating contact area, and boundary lubrication by synovial fluid, on cartilage friction. Osteoarthritis Cartilage 2008;16:1220–7.
[42] Pawaskar SS, Jin ZM, Fisher J. Modelling of fluid support inside articular cartilage during sliding. Proc Inst Mech Eng J: J Eng Tribol 2007;221:165–74.
[43] Willett TL, Whiteside R, Wild PM, Wyss UP, Anastassiades T. Artefacts in the mechanical characterization of pocine articular cartilage due to freezing. Proc Inst Mech Eng H: J Eng Med 2005;219:23–9.
[44] Hosoda N, Sakai N, Sawae Y, Murakami T. Depth-dependence and time-dependence in mechanical behavior of articular cartilage in unconfined compression test under constant total deformation. J Biomech Sci Eng 2008; 3:209–20.
[45] Wu JZ, Herzog W, Epstein M. Evaluation of the finite element software ABAQUS for biomechanical modelling of biphasic tissues, technical note. J Biomech 1998;31:165–9.
[46] Pawaskar SS, Jin ZM, Fisher J. Robust and general method for determining surface fluid flow boundary conditions in articular cartilage contact mechanics modeling. J Biomech Eng—Trans ASME 2010;132:3.
[47] Krishnan R, Park S, Eckstein F, Ateshian GA. Inhomogeneous cartilage properties enhance superficial interstitial fluid support and frictional properties, but do not provide a homogeneous state of stress. J Biomech Eng—Trans ASME 2003;125:569–77.
[48] Thambyah A, Broom N. Micro-anatomical response of cartilage-on-bone to compression: mechanisms of deformation within and beyond the directly loaded matrix. J Anat 2006;209:611–22.
[49] Guilak F, Mow VC. The mechanical environment of the chondrocyte: a biphasic finite element model of cell–matrix interactions in articular cartilage. J Biomech 2000;33:1663–73.
[50] Williamson AK, Chen AC, Masuda K, Thonar EJMA, Sah RL. Tensile mechanical properties of bovine articular cartilage: variations with growth and relationships to collagen network components. J Orthop Res 2003;21: 872–80.
[51] Klein TJ, Caudhry M, Bae WC, Sah RL. Depth-dependent biomechanical and biochemical properties of fetal, newborn, and tissue-engineered articular cartilage. J Biomech 2007;40:182–90.